Research Article | Open Access

Journal of Materials Informatics

Li *et al. J. Mater. Inf.* **2026**, *6*, 58 **DOI:**10.20517/jmi.2026.51

Rapid design of high-strength high-conductivity copper alloys via machine learning and NSGA-II multi-objective optimization

Yuhong Li[1], Jing Xu[1], Bo Guan[1,*], Dan Wu[1], Yushuai Han[1], Xiankang Pan[1], Huadi Xu[1], Zhi Hu[2,*], Guohong Ma[2], Qiang Hu[1,*]

Keywords:
Cu-Ni-Co-Si-Mg-Ag alloy, machine learning, multi-objective optimization

Citation: Li, Y.; Xu, J.; Guan, B.; Wu, D.; Han, Y.; Pan, X.; Xu, H.; Hu, Z.; Ma, G.; Hu, Q. Rapid design of high-strength high-conductivity copper alloys via machine learning and NSGA-II multi-objective optimization. *J. Mater. Inf.* **2026**, *6*, 58. https://dx.doi.org/10.20517/jmi.2026.51

Received: 8 Jul 2026
First Decision: 21 Sep 2026
Revised: 16 Nov 2026
Accepted: 17 Nov 2026
Published: 25 Nov 2026

Academic Editor:
Xiang-Dong Ding
Copy Editor:
Pei-Yun Wang
Production Editor:
Pei-Yun Wang

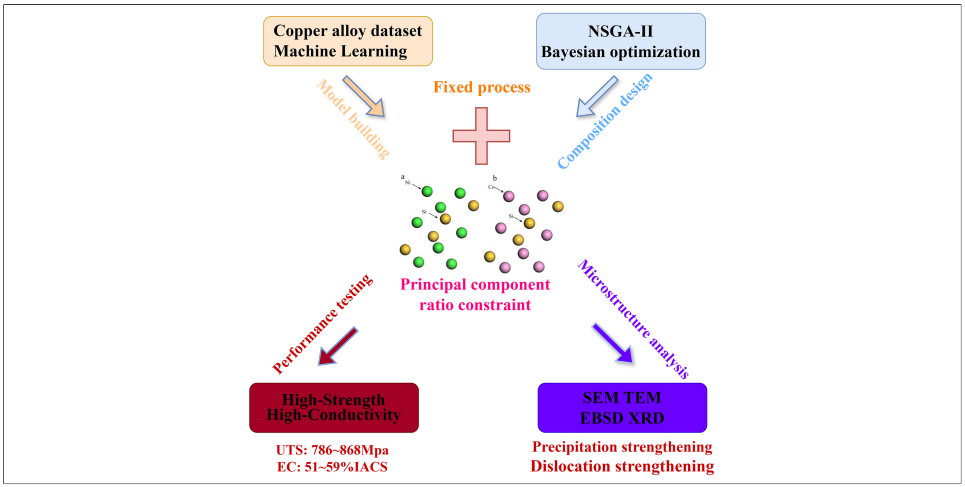

Abstract

The strength and conductivity properties of Cu–Ni–Si alloys are synergistically regulated by composition and thermomechanical processing. However, the global design of Cu–Ni–Si alloys within the multi-dimensional composition-processing space is bottlenecked by dual challenges: high-dimensional complexity and the strength–conductivity performance trade-off. To resolve these challenges, the present study integrates machine learning, multi-objective optimization and empirical knowledge into a novel paradigm for rapid alloy design. First, to efficiently generate the Pareto front in the Ni–Co–Si–Mg–Ag–Cr composition space, a gradient boosting regression (GBR) surrogate model is constructed and embedded into a multi-objective optimization algorithm (Non-dominated Sorting Genetic Algorithm-II). Guided by previous process development experience, the multi-pass rolling–aging process is fixed within an optimal window, coupling a stepwise strategy of composition optimization with fixed processing parameters. After only seven sets of experiments, composition screening uncovered an outstanding Cu–0.65Ni–1.65Co–0.44Si

[1]Jiangxi Key Laboratory of Advanced Copper-based Materials, Institute of Materials and Intelligent Manufacturing, Jiangxi Academy of Sciences, Nanchang 330096, Jiangxi, China.
[2]School of Advanced Manufacturing, Nanchang University, Nanchang 330031, Jiangxi, China.

***Correspondence to:** Dr. Bo Guan, Prof. Qiang Hu, Jiangxi Key Laboratory of Advanced Copper-based Materials, Institute of Materials and Intelligent Manufacturing, Jiangxi Academy of Sciences, Nanchang 330096, Jiangxi, China. E-mail: bguan2022@163.com; huqiang1225@163.com; Prof. Zhi Hu, School of Advanced Manufacturing, Nanchang University, Nanchang 330031, Jiangxi, China. E-mail: huzhi@ncu.edu.cn

–0.09Mg–0.46Ag alloy with a tensile strength of 868.63 MPa and a conductivity of 59.2% in International Annealed Copper Standard units. Combining the high strength of reported copper alloys with improved electrical conductivity, this alloy overcomes the performance bottleneck of the existing copper alloys and demonstrates excellent application potential. Next, the synergistic mechanism by which trace Ag promotes the formation of nanoscale δ-$(Ni,Co)_2Si$ precipitates and purifies solutes in the matrix is elucidated, along with the intrinsic mechanism underlying precipitate strengthening and the simultaneous strength–conductivity improvement through composition design. Overall, this study provides a new perspective for composition design of precipitation-strengthened alloys.

INTRODUCTION

The optimization of conductive materials for high-end manufacturing applications, such as current 5G communications, integrated circuit lead frames and high-voltage connectors in new energy vehicles, is currently advancing from single-performance optimization to synergistic "ultra-high strength and high conductivity" optimization. Expensive and toxic beryllium copper (Be–Cu; C17200)[1,2] and performance-limited copper–iron alloys (Cu–Fe; C19400)[3-5] can potentially be replaced by copper–nickel–silicon (Cu–Ni–Si) alloys, typical precipitation-strengthened Cu alloys with tensile strengths exceeding 800 MPa and electrical conductivities (ECs) reaching 45%-52% in International Annealed Copper Standard (IACS) units. However, the development and deployment of large models has increased the demand for computing power, and high-current connectors are required for new high-voltage energy platforms, imposing stringent performance requirements on the high-strength and high-conductivity Cu alloys used in power transmission systems. Although the existing commercial grades such as C70250[6-8] and C70350[9-12] have preliminarily balanced the strength–EC trade-off, the composition ratios of traditional Cu–Ni–Si alloys have approached their physical limits. Rapid, accurate design of alloys that meet the target performance within a multi-dimensional composition space would overcome the material bottlenecks and support the development of next-generation power electronic devices.

In recent years, combined machine learning and multi-objective optimization approaches have been applied to alloy-composition design. For example, Zhang *et al.* designed a Cu–1.3Ni–1.4Co–0.56Si–0.03Mg alloy through machine learning and Bayesian multi-objective optimization, achieving a tensile strength of 858 MPa and an EC of 47.6% IACS[11]. Li *et al.* developed a Cu–2.1Ni–0.80Co–0.74Si–0.22Mg-0.11Ti alloy with a tensile strength of 911.4 MPa and an EC of 44.37% IACS[12]. A comprehensive literature review revealed a prominent strength–conductivity trade-off bottleneck at tensile strengths above 800 MPa in the existing Cu–Ni–Si alloys: at this strength, the EC is generally upper-limited to 52% IACS. This ceiling is mainly attributable to the strengthening mechanisms of traditional high-strength copper alloys, such as solid-solution and grain-refinement strengthening, which inevitably reduce the EC. Although elements such as chromium (Cr), magnesium (Mg) and silver (Ag) synergistically improve the comprehensive strength–conductivity performance of copper alloys[11-14], precise optimization of the composition combination in the Ni–Co–Si–Mg–Ag–Cr composition space is essential for substantially increasing the EC while maintaining high strength.

Meanwhile, Cu–Ni–Si alloys are typical age-hardening alloys that require rolling and aging processes, in addition to an appropriate chemical composition, for synergistic regulation of strength and conductivity. In general, both properties can be simultaneously improved by increasing the number of rolling–aging passes. Alternating multi-pass rolling and aging increases the density of second-phase particles, thereby reducing electron scattering from solute atoms in the matrix and optimizing the EC. However, if all complex process parameters (e.g., solution temperature/duration, hot rolling temperature and total rolling reduction) are incorporated into a machine-learning model, the dramatic increase in feature dimensions and training difficulty will raise both the model complexity and prediction uncertainty.

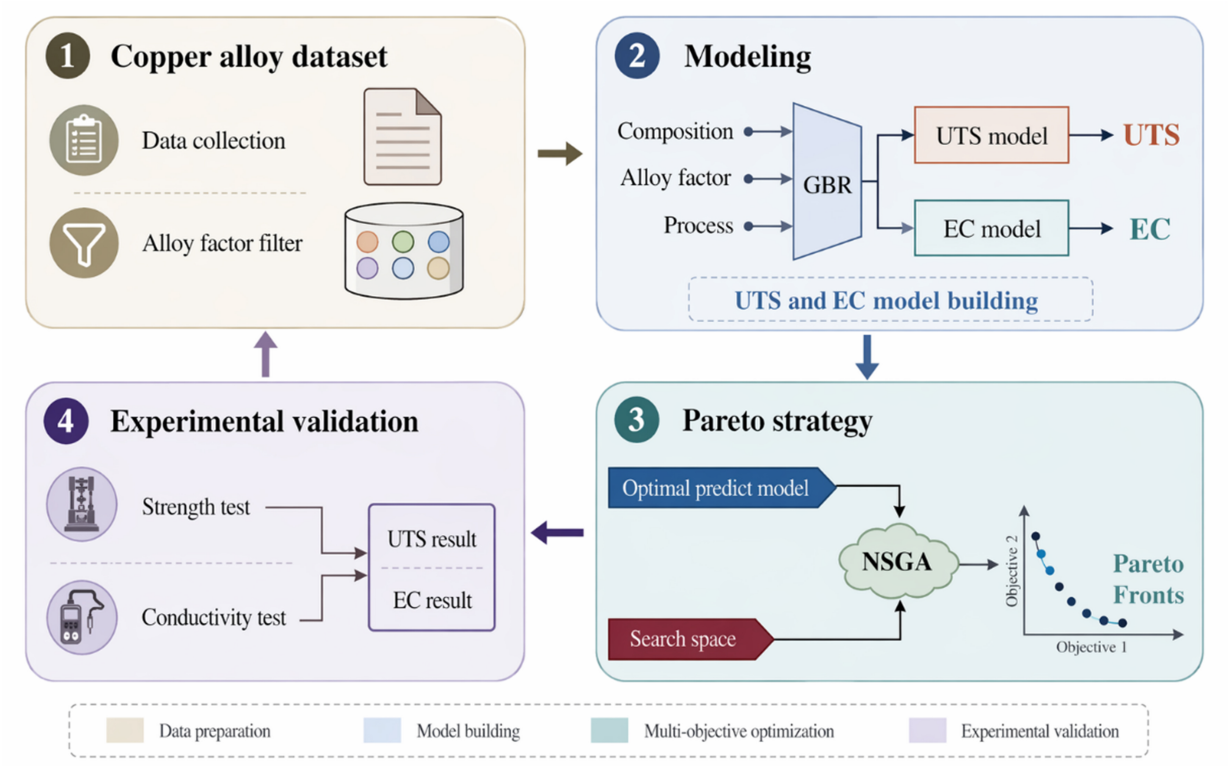

Figure 1. Flowchart of the overall design. GBR: Gradient boosting regression; UTS: ultimate tensile strength; EC: electrical conductivitie; NSGA: Non-dominated Sorting Genetic Algorithm.

Based on previous research, this paper proposes an integrated design strategy that optimizes the composition through multi-objective optimization with machine learning and adopts our previously established optimized multi-pass rolling–aging scheme in the thermomechanical processing route[12,15]. First, the optimal solution in the composition space is efficiently searched using Non-dominated Sorting Genetic Algorithm-II (NSGA-II)[16] embedded with a gradient boosting regression (GBR) surrogate model. The objective is the simultaneous improvement of EC and strength. The process parameters, taken from previous studies, are fixed within the optimal multi-pass rolling–aging window. After only seven rounds of experimental verification, this strategy successfully designed a Cu alloy with a tensile strength of 868.63 MPa and an EC of 59.2% IACS, confirming the reliability of the strategy for efficient and rapid design of Cu alloys.

MATERIALS AND METHODS

Overall design strategy

To rapidly and efficiently optimize Cu alloy compositions with enhanced precipitation hardening properties, the strategy combines data-driven analysis, model building, intelligent optimization and experimental validation. The workflow proceeds as follows: (1) curation of a comprehensive dataset of copper alloys; (2) construction of a machine-learning prediction model; (3) identification of the Pareto-optimal solution set using the NSGA-II algorithm; and (4) validation of the design results through experimental fabrication and multi-scale characterization. The complete technical workflow is illustrated in Figure 1. The individual steps are detailed below.

(1) Copper-alloy data collection: An effective machine-learning algorithm requires high-quality data. With reference to literature-reported dataset sizes and patents on machine learning-aided design of Cu alloys, a high-quality dataset was constructed from 412 preprocessed Cu-alloy records covering typical alloy systems such as Cu–Ni–Si, Cu–Ni–Co–Si–Mg, Cu–Cr and Cu–Ag, which represents a reasonable design scale[17-21].

Input features are the mass fractions of six elements - Ni, Co, Si, Mg, Ag and Cr - and the processing sequence (solution treatment → first rolling → first aging → second rolling → second aging). The output targets are ultimate tensile strength (UTS) and EC.

(2) Machine-learning model development: To improve its accuracy and physical interpretability, the model was incorporated with material descriptors such as second ionization energies and atomic radii. The optimal combination of alloying elements was identified through exhaustive screening using a random forest algorithm. Subsequently, the chemical composition, alloying elements and process parameters were integrated to form a multi-dimensional feature space. The hyperparameters were optimized via grid search and cross-validation. In trials of various machine-learning algorithms, GBR[22] was identified as the optimal model for predicting the UTS and EC.

(3) NSGA-II multi-objective optimization: After constructing the best-performing predictive model, the Pareto-optimal solution set was found using the NSGA-II algorithm. The quality of the solution set was further improved through Bayesian optimization of the key hyperparameters (population size, crossover probability, mutation probability and PM distribution index). Under the objective of minimizing the negative hypervolume[23], the optimal combination of hyperparameters was determined after 150 iterations (with 300 generations of evolutionary search per iteration). Subsequently, full 3000-generation evolutionary searches were conducted across three composition subspaces (Cu–Ni–Co–Si–Mg–Cr, Cu–Ni–Co–Si–Mg–Ag and Cu–Ni–Co–Si–Mg–Ag–Cr) on output solution sets that fully cover the Pareto front.

(4) Experimental validation and microstructural characterization: From the output set of Pareto solutions, a constraint was imposed on the (Ni+Co)/Si ratio (4.0-5.4) and seven representative compositions were screened for melting and preparation under performance thresholds of UTS ≥ 850 MPa and EC ≥ 52% IACS. After multi-step thermomechanical treatment, the mechanical properties and ECs of the alloys were systematically tested, isolating three representative alloys (Cr-containing, Ag-containing and Cr–Ag-containing) for further multi-scale characterization using scanning electron microscopy (SEM), electron backscatter diffraction (EBSD), X-ray diffraction (XRD) and transmission electron microscopy (TEM). These analyses revealed the intrinsic relationship between composition, microstructure and properties.

Experimental methods

Material preparation

The designed alloys were fabricated via vacuum induction melting under argon protection. High-purity raw materials - electrolytic copper (99.999 wt%), Ni (99.99 wt%), Co (99.99 wt%), Si (99.99 wt%), Mg (99.95 wt%), Cr (99.99 wt%) and Ag (99.99 wt%) - were formulated and melted to the designed chemical compositions, obtaining ingots with an approximate size of 30 mm × 30 mm × 50 mm. The thermomechanical processing route is detailed in Supplementary Figure 1. Furthermore, the actual chemical composition of the optimal alloy was confirmed by inductively coupled plasma–optical emission spectrometry. The corresponding data are listed in Supplementary Table 1.

Property test and microstructural observation

The mechanical performance of the alloys was assessed on a CMT5205 universal testing machine under a constant tensile rate of 2 mm/min. To ensure data reliability, each specimen was independently tested in triplicate and averaged to obtain the reported value. During the testing process, the plastic strain was accurately measured with a strain gauge. EC of each sample was determined from the resistance measured with a ZY9987 digital micro-ohmmeter at 25 °C and reported as the average of triplicate measurements. For microstructural characterization, SEM, EBSD and TEM samples were prepared using electropolishing, argon ion milling and ion beam thinning, respectively. XRD was performed over the range $2\theta = 30°$-$95°$.

Based on prior research methodologies, the machine-learning phase of the system incorporated seven key alloy descriptors, including atomic radius differences and variances of the second ionization energy. The optimal predictive model for UTS and EC was ultimately developed through exhaustive screening using random forest and multi-algorithm comparisons, combined with cross-validation to optimize the hyperparameters [Supplementary Table 2].

RESULTS AND DISCUSSION

Machine learning and rational analysis of key factors

Machine learning

Figure 2A and B show the optimal combinations of alloying factors obtained via exhaustive screening with random forest in the UTS and EC models, respectively. The alloying factors are (GPa, delta_r, sigma2 and W) in the UTS model and (GPa, delta_r and W) in the EC model respectively. Subsequently, the prediction errors of different feature combinations were compared using an artificial neural network[24], identifying the optimal input as "element content + alloying factors + process parameters" [Supplementary Figure 2]. Ultimately, the UTS model was input with the alloying element contents, the alloying factors, GPa, delta_r, sigma2 and W, and the process parameters. The EC model was input with the alloying element contents, the alloying factors, GPa, delta_r and W, and the process parameters.

Finally, the prediction accuracies and robustness levels of multiple machine-learning algorithms[25-28] [Supplementary Tables 3-7] were comprehensively compared, and the model selection results are presented in Figure 2C-F. Figure 2C and D shows the coefficients of determination (R^2) and root mean squared errors (RMSEs) of the different algorithms on the test set under a 2:8 training:test split, and Figure 2E and F display the training-set RMSEs of each algorithm derived from 10-fold cross-validation. As GBR outperformed the other algorithms in both prediction accuracy and stability, it was selected as the optimal model for further analysis. The RMSEs of the UTS and EC predictions from this model were 57.89 MPa and 6.12% IACS, respectively [Figure 2G and H].

Key factors analyses

The physical mechanisms underlying the influence of the optimal alloying elements on material performance were elucidated through a SHapley Additive exPlanations (SHAP) interpretability[29] analysis of the UTS and EC models [Figure 3]. The UTS increase in Cu–Ni–Co–Si alloys is primarily credited to the effect of nanoscale $(Ni,Co)_2Si$ precipitation phases formed during the aging process. The SHAP results indicate that the variance in sigma2 carries the highest weight and is negatively correlated with UTS, reflecting subtle differences among the electronic structures of Ni, Co and Cu. Sigma2 may be statistically correlated with the inhomogeneity of local chemical-bonding environments, thereby influencing the dislocation–precipitate interactions. Nevertheless, this interpretation is only hypothesized from the model feature importance and awaits atomic-scale validation. The high positive association between GPa and UTS validates the contribution of the precipitates as hard intermetallic compounds. The higher-order terms of W capture the strong covalent bonding within the precipitate phase, which influences the extent to which the precipitate can pin dislocations during deformation. The delta_r also manifests as a positive gain in the UTS model. The solute strengthening is driven by distortion caused by solute atoms, whereas delta_r determines the congruent strain field between the precipitate phase and the matrix.

In stark contrast to the UTS model, the EC model is dominated by the compressibility factor delta_r; specifically, EC is very strongly negatively correlated with this factor. EC depends on the mean free path of electrons. In the Cu–Ni–Co–Si system, the delta_r between Cu and the Ni, Co and Si atoms is the primary source of scattering. The SHAP results clearly reveal the importance of the matrix purification effect: the

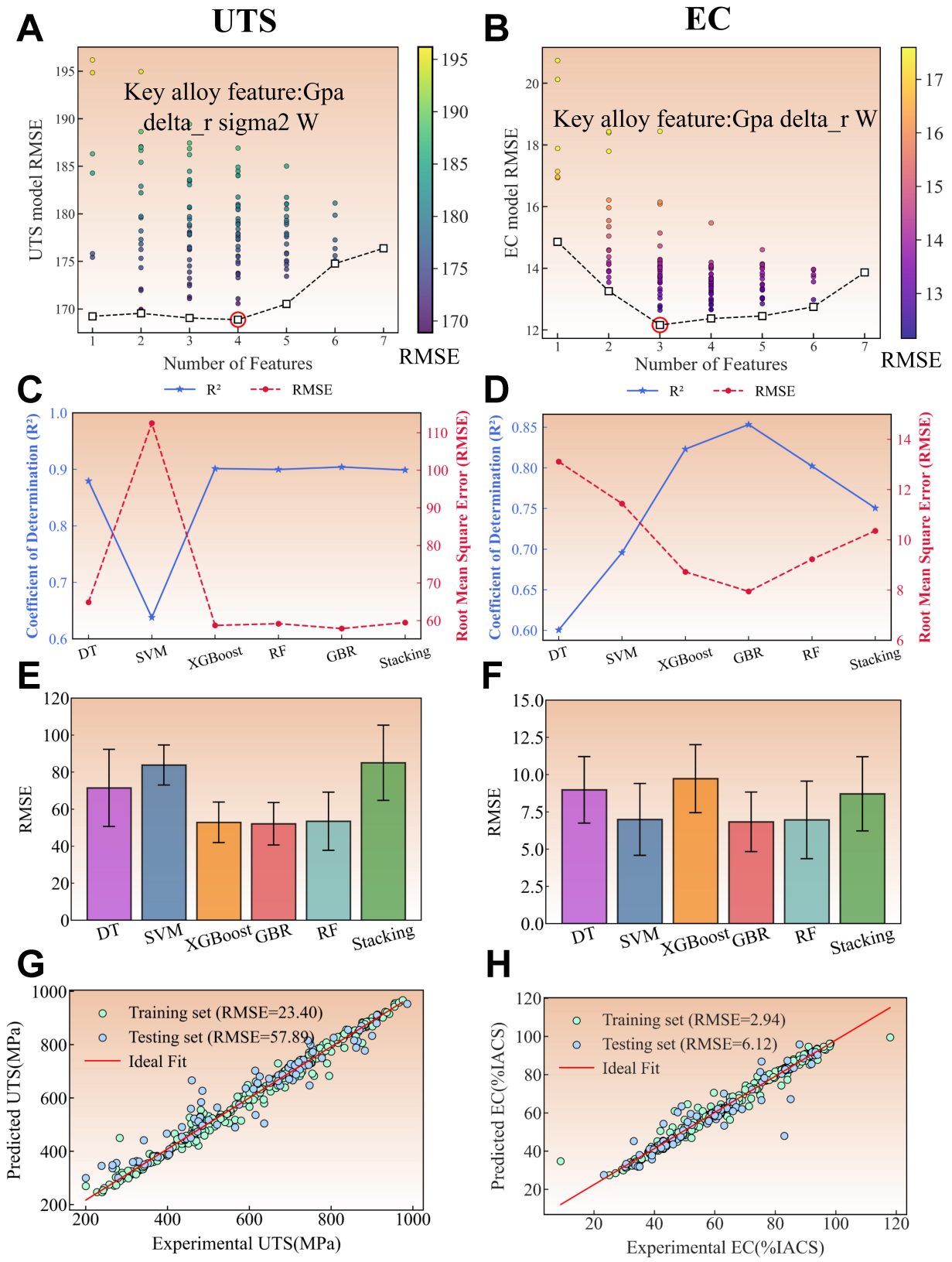

Figure 2. Final training results of machine learning models for UTS and EC. (A and B) Results of exhaustive screening of alloy factors using random forest algorithm; (C and D) Comparison of the partitioning effects of training and test sets (2-8 split) for each algorithm; (E and F) The 10-fold cross-validation results of each algorithm; (G and H) The optimal prediction models for UTS and EC. UTS: Ultimate tensile strength; EC: electrical conductivitie; RMSE: root mean squared error; R^2: coefficient of determination; DT: decision tree; SVM: support vector machine; XGBoost: eXtreme gradient boosting; RF: random forest; GBR: gradient boosting regression; IACS: International Annealed Copper Standard.

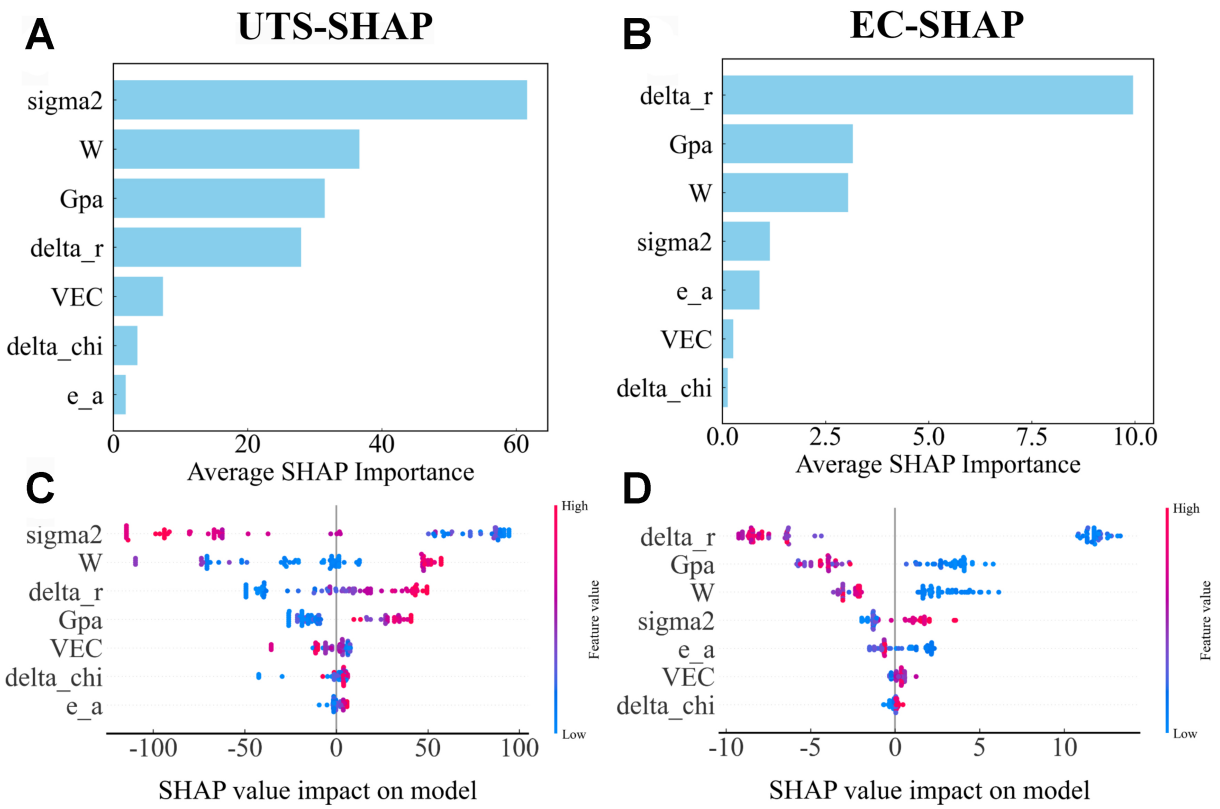

Figure 3. SHAP analysis results of each alloy factor. (A and B) Alloy factor SHAP importance distribution chart; (C and D) Alloy factor contribution chart. SHAP: SHapley Additive exPlanations; UTS: ultimate tensile strength; EC: electrical conductivitie.

Table 1. Range of ingredient content (wt%)

Cu	Ni	Co	Si	Mg	Ag	Cr	Space
Bal	0.1-3.0	0.1-2.0	0.1-2.0	0.01-0.5	0	0-2.0	Cu–Ni–Co–Si–Mg–Cr
Bal	0.1-3.0	0.1-2.0	0.1-2.0	0.01-0.5	0-2.0	0	Cu–Ni–Co–Si–Mg–Ag
Bal	0.1-3.0	0.1-2.0	0.1-2.0	0.01-0.5	0-2.0	0-2.0	Cu–Ni–Co–Si–Mg–Ag–Cr

purity of the matrix is restored only when the size-mismatched solute atoms become fully incorporated into the $(Ni,Co)_2Si$ precipitation phase during the aging process. Meanwhile, the effects of GPa and W on EC are negative but minor, typically masked by distortion scattering caused by residual solutes during the precipitation-hardening-dominated stage.

Multi-objective optimization and reliability analysis of the pareto set

Multi-objective optimization

After identifying a GBR model that balances the accuracy and robustness of the UTS and EC models, global searches in three composition subspaces (Cu–Ni–Co–Si–Mg–Cr, Cu–Ni–Co–Si–Mg–Ag and Cu–Ni–Co–Si–Mg–Ag–Cr) were conducted using the NSGA-II algorithm. The specific steps are detailed below:

Define the search space: This step sets the mass-fraction ranges of the elements (e.g., Ni, Co, Si, Mg, Cr and Ag in Table 1) and fixes the solution treatment, aging and rolling process parameters [Supplementary Table 8].

Set the optimization objectives: The objective is to simultaneously maximize the UTS and EC.

Perform an NSGA-II search: This step efficiently identifies the set of Pareto-frontier solutions in the composition space, covering three combinations: Cu–Ni–Si–Co–Mg–Cr, Cu–Ni–Si–Co–Mg–Ag and Cu–Ni–Si–Co–Mg–Ag–Cr.

Output the candidate window: This step provides a reliable design space for component selection, which will be experimentally validated.

To improve the overall quality of the Pareto solution set, the main NSGA-II search was preceded by Bayesian hyperparameter optimization, which aims to maximize the hypervolume metric using the population size, crossover probability, crossover distribution index (crossover_eta), mutation probability and mutation distribution index (mutation_eta) as optimization variables. The process was run through 150 iterations within the predefined search range [Table 2]. Figure 4A-C illustrates the Bayesian optimization process, which selects the optimal NSGA-II configuration that minimizes the hypervolume (i.e., minimizes the negative hypervolume). The NSGA-II details of each space are provided in Supplementary Table 9. Figure 4D-F presents the Pareto fronts comprising 74, 72 and 100 non-dominated solutions, respectively, after 3,000 consecutive generations using the optimized hyperparameters. The performances of the Pareto front solution sets[30] were comprehensively ranked using the Technique for Order of Preference by Similarity to Ideal Solution (TOPSIS) method, which is determined by ($w_{UTS} = w_{EC} = 0.5$):

$$UTS_{norm} = UTS_i/UTS_{Max} \quad EC_{norm} = EC_i/EC_{Max} \tag{1}$$

$$d_i^+ = \sqrt{w_{UTS}(UTS_{norm,i} - 1)^2 + w_{EC}(EC_{norm,i} - 1)^2} \tag{2}$$

$$d_i^- = \sqrt{w_{UTS}(UTS_{norm,i} - 0)^2 + w_{EC}(EC_{norm,i} - 0)^2} \tag{3}$$

$$\text{TOPSIS Score}_i = \frac{d_i^-}{d_i^+ + d_i^-} \tag{4}$$

Pareto set analyses

The reliability of the Pareto solution set was checked through a local composition-property correlation analysis and quadratic fitting on the Cu–Ni–Co–Si–Mg–Ag alloy composition combinations. The results are presented in Figure 5.

In a scatter plot analysis of the Ni, Co, Si, Mg and Ag contents *vs.* UTS and EC properties within the solution sets, all solutions adhered to metallurgical principles; that is, increasing the content of the alloying element enhanced the strength but decreased the EC.

Furthermore, the influence patterns of the primary alloying elements (Ni, Co and Si) on the alloy properties fully aligned with the precipitation-strengthening mechanism of Cu–Ni–Co–Si-based alloys. Specifically, the ratio of Ni, Co and Si contents directly regulates the formation of the $(Ni,Co)_2Si$ phase. The Co and Ni contents were positively correlated with alloy strength (R^2 = 0.93 and 0.7, respectively) and negatively correlated with EC (R^2 = -0.91 and -0.61, respectively). The strong correlations for Co indicate that Co is the most influential factor of both UTS and EC. Notably, as Co is more soluble in Cu than in Ni, it can sustainably contribute to precipitation strengthening across a broader composition range than the other elements. Furthermore, as indicated in prior research, minor Co additions significantly diminish the interfacial energy between the Cu matrix and precipitates, and a low interfacial energy accelerates the generation of the $(Ni,Co)_2Si$ precipitation phase.

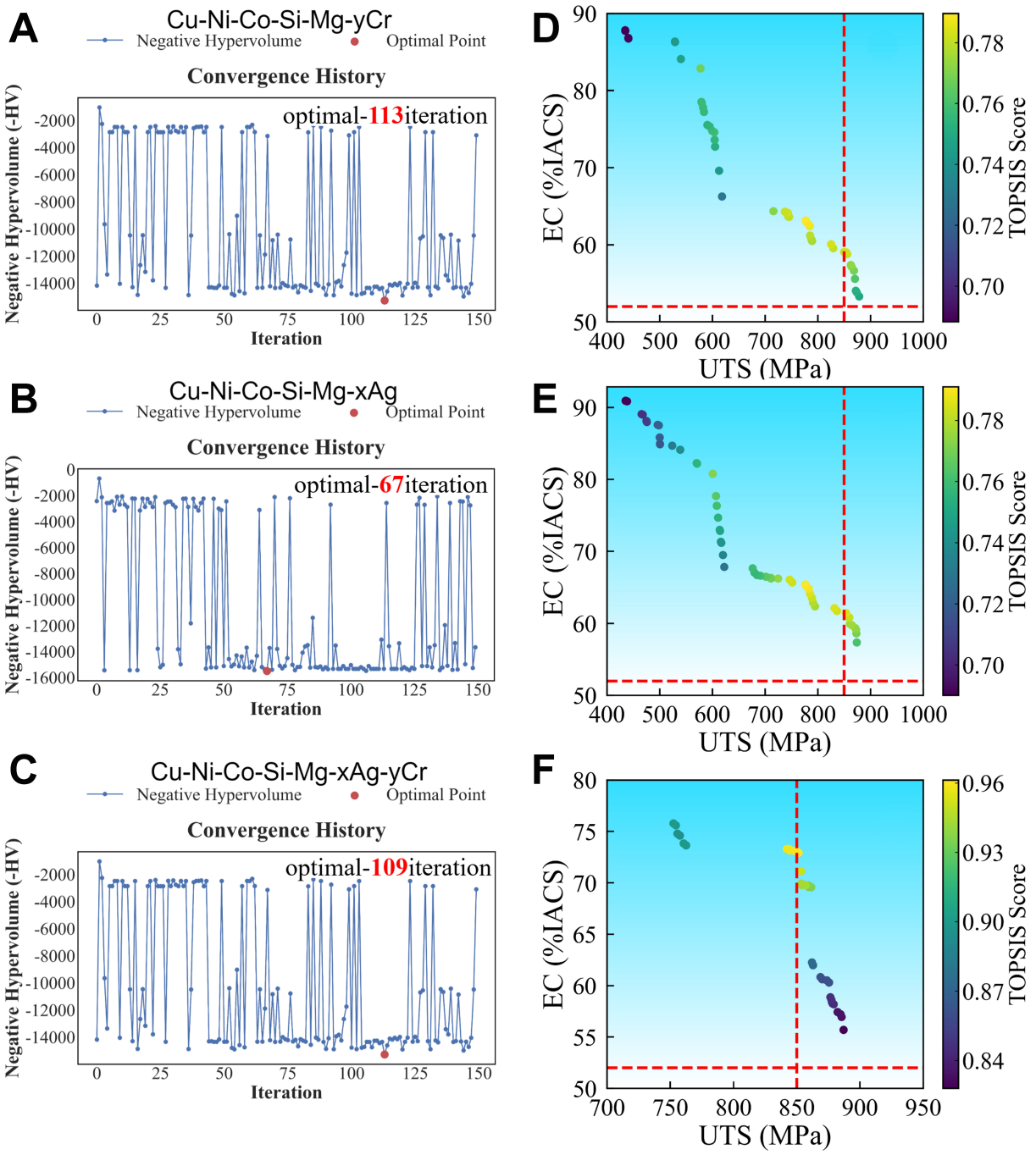

Figure 4. Bayesian iterative parameter process and pareto solution set. (A and D) Cu–Ni–Co–Si–Mg–Cr space; (B and E) Cu–Ni–Co–Si–Mg–Ag space; (C and F) Cu–Ni–Co–Si–Mg–Ag–Cr space. EC: Electrical conductivitie; IACS: International Annealed Copper Standard; TOPSIS: Technique for Order of Preference by Similarity to Ideal Solution; UTS: ultimate tensile strength.

Table 2. NSGA-II algorithm hyperparameters search space

Pop_size	Crossover_prob	Crossover_eta	Mutation_prob	Mutation_eta
(30,100)	(0.6,0.95)	(5,30)	(0.01,0.3)	(5,30)

NSGA-II: Non-dominated Sorting Genetic Algorithm-II.

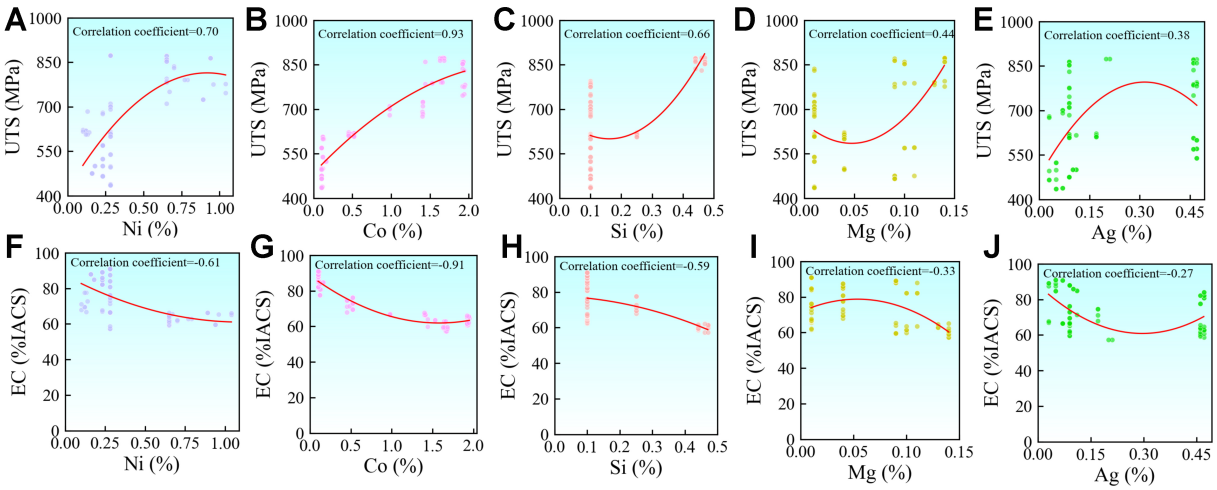

Figure 5. Local correlation analysis of composition and properties within the Pareto optimal set. (A-E) Distribution of the effects of Ni, Co, Si, Mg, Ag content and UTS; (F-J) Distribution of the effects of Ni, Co, Si, Mg, Ag content and EC. UTS: Ultimate tensile strength; EC: electrical conductivitie; IACS: International Annealed Copper Standard.

Table 3. Composition of the seven recommended alloys

Id	Si (wt%)	Mg (wt%)	Ni (wt%)	Ag (wt%)	Co (wt%)	Cr (wt%)	Space
1	0.46	0.09	0.65	0	1.72	0.47	Cu–Ni–Co–Si–Mg–Cr
2	0.47	0.14	0.25	0	1.71	0.56	Cu–Ni–Co–Si–Mg–Cr
3	0.44	0.09	0.65	0.46	1.65	0	Cu–Ni–Co–Si–Mg–Ag
4	0.47	0.1	0.65	0.46	1.44	0	Cu–Ni–Co–Si–Mg–Ag
5	0.48	0.14	0.65	0.09	1.72	0.35	Cu–Ni–Co–Si–Mg–Ag–Cr
6	0.46	0.14	0.23	0.47	1.97	0.33	Cu–Ni–Co–Si–Mg–Ag–Cr
7	0.45	0.14	0.29	0.09	1.72	0.1	Cu–Ni–Co–Si–Mg–Ag–Cr

Experimental verification and changes in composition and property

Experimental verification

As the strengthening mechanism of Cu–Ni–Co–Si alloys primarily relies on precipitation hardening via the δ-$(Ni,Co)_2Si$ phase[31-33], sufficient formation of the precipitate phase is important. To this end, the entire Pareto set was subjected to the constraint (Ni+Co)/Si mass ratio = 4.0-5.4, and the proxy model predictions were constrained to UTS ≥ 850 MPa and EC ≥ 52% IACS. Under these constraints, the TOPSIS scores of the solution sets corresponding to the Cu–Ni–Co–Si–Mg–Cr, Cu–Ni–Co–Si–Mg–Ag and Cu–Ni–Co–Si–Mg–Ag–Cr spaces should exceed 0.59, 0.59 and 0.49, respectively. After a two-stage screening process, seven representative alloy compositions were ultimately obtained as detailed in Table 3.

Although machine learning globally optimizes the alloy composition to elevate both its strength and EC, the rolling and aging treatments decisively influence the final properties of age-hardened Cu alloys. To maximize the combination of high strength and high EC (targeting UTS ≥ 850 MPa, EC ≥ 52% IACS), the machine-learning results were verified through multi-step thermomechanical processing. This verification choice was decided based on previous experience.

The complex rolling–aging process was not directly applied in the composition design stage for two reasons. First, although multiple rolling–aging cycles can significantly improve the alloy properties, reliable modeling is rendered difficult by the limited availability of existing high-quality data. Second, increasing the number of

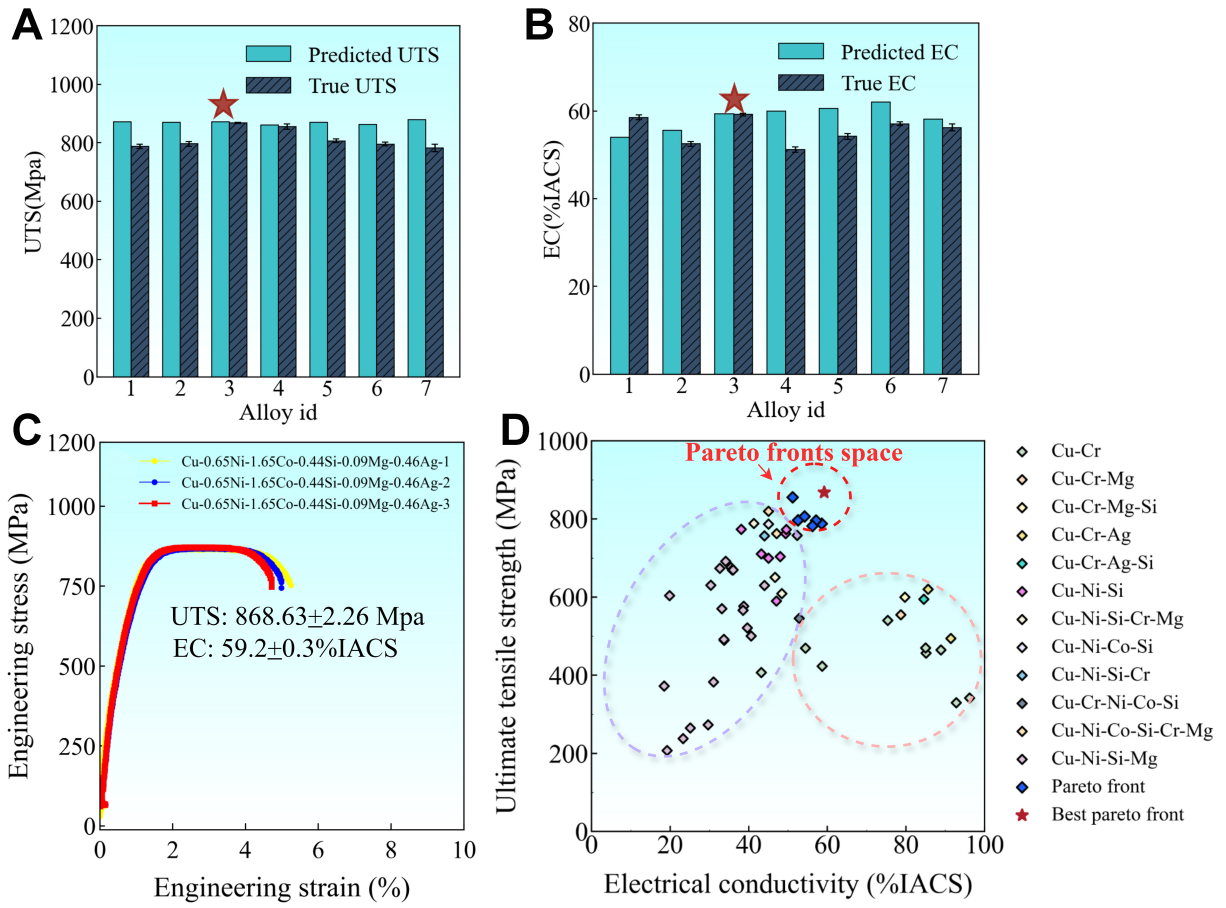

Figure 6. Comparison between predicted and experimental values of the seven alloys, as well as the stress-strain curve of the alloy with optimal performance. (A and B) Predicted and experimental values of UTS and EC; (C) Cu–0.65Ni–1.65Co–0.44Si–0.09Mg–0.46Ag alloy stress-strain curve; (D) Performance comparison between the alloys designed in this work and previously reported alloys. UTS: Ultimate tensile strength; EC: electrical conductivitie; IACS: International Annealed Copper Standard.

process parameters raises the feature dimension and training difficulty, which tends to cause overfitting.

Supplementary Figure 3 shows the tensile curves and mechanical properties of the seven designed alloy samples. Figure 6A and B plot the predicted *vs.* actual UTS and EC values, respectively, of the seven alloys. The prediction errors in the UTS and EC of the seven alloy samples are provided in Supplementary Table 10. The 3-alloy Cu–0.65Ni–1.65Co–0.44Si–0.09Mg–0.46Ag delivered the best overall performance, although the prediction errors were low overall. Figure 6C shows the stress–strain curves of the 3-alloy obtained in three independent tensile tests, and Figure 6D compares the performance of the copper alloy designed through the Pareto set method with those of previously reported alloys[31-36]. The best-performing copper alloy clearly surpasses the reported copper alloys in terms of the combined strength–conductivity index.

Composition and property analyses

Ni, Co and Si are the core elements of the Cu–Ni–Co–Si precipitation-hardening alloy system. The contents and ratios of these elements directly determine the volume fraction, size distribution and strengthening efficiency of the precipitated phases. To quantify the effects of these factors on strength and EC, the relationships among the total Ni+Co+Si content, (Ni+Co)/Si mass ratio, UTS and EC of the seven experimental alloy systems were systematically analyzed. The results are shown in Figure 7. Noticeable deviations appear between the actual and nominal compositions of the alloys. Therefore, the total Ni+Co+Si

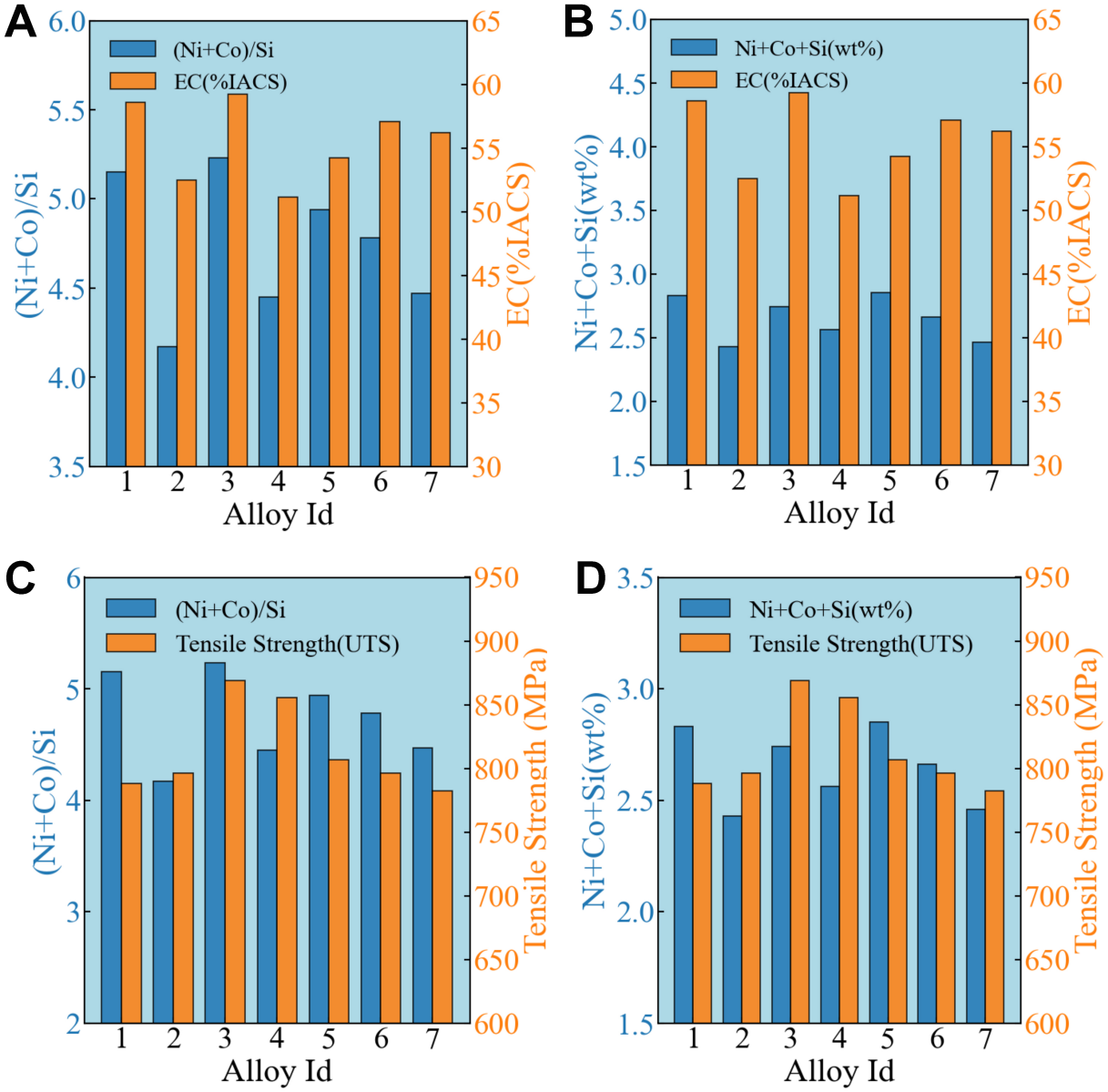

Figure 7. Analysis of the Relationship between Ni, Co and Si content combinations and performance variations. (A and C) Distribution of the effects of (Ni+Co)/Si ratio on UTS and EC; (B and D) Distribution of the effects of total mass fraction of Ni+Co+Si on UTS and EC. UTS: Ultimate tensile strength; EC: electrical conductivitie; IACS: International Annealed Copper Standard.

content and (Ni+Co)/Si mass ratios were calculated as ranges, assuming that such compositional deviations are within an acceptable range.

Within the same category of alloying elements, the tensile strength of the alloy generally increased with increasing total contents of Ni, Co and Si [Figure 7D]. This result is explained by the positive association between the overall Ni, Co and Si content and number of precipitates that can be formed. The volume fraction of these precipitates majorly influences the mechanical properties of the alloy. Increasing the number of precipitates enhances the strengthening effect of the precipitated phases, thereby increasing the tensile strength of the alloy. Consequently, the trend in UTS closely parallels the variation in total content of Ni+Co+Si.

However, the precipitation strengthening of the alloy is not governed solely by the total Ni+Co+Si content. As observed in Figure 7C, an appropriate (Ni+Co)/Si ratio is equally critical for tensile strength. When the alloying element species are fixed, an excessively high or excessively low (Ni+Co)/Si ratio will reduce the alloy strength. Accordingly, both the total Ni+Co+Si content and (Ni+Co)/Si ratio should be simultaneously regulated during the alloy composition design.

Meanwhile, the EC is primarily determined by the total solute content (Ni+Co+Si). Increasing the total content enhances electron scattering and hence decreases the EC [Figure 7A and B]. However, in alloys with comparable total contents, the (Ni+Co)/Si mass ratio plays a crucial role. For instance, when the ratio reaches approximately 5.2, Ni and Co form nearly complete precipitates with Si, substantially reducing the residual solutes in the matrix and thereby maintaining a high EC. The 2-alloy possesses the lowest (Ni+Co)/Si ratio but also the lowest absolute total solute content, resulting in minimal lattice distortion and the highest EC among the alloys.

In the Cu–0.65Ni–1.65Co–0.44Si–0.09Mg–0.46Ag alloy engineered through machine learning and multi-objective optimization, the total Ni+Co+Si content is 2.74 wt% and the (Ni+Co)/Si ratio is 5.23. The exceptional properties of this alloy stem primarily from the precise ratio of Ni, Co and Si, coupled with the synergistic effects of Mg and Ag. The Ag additive further enhances the UTS and EC of the alloy. Machine learning and multi-objective optimization techniques played a pivotal role in recommending this composition. Setting the (Ni+Co)/Si ratio range within the potential Pareto solution set (4.0-5.4) and targeting UTS and EC values of 850 MPa and 52% IACS, respectively, the alloy composition meeting the performance requirements was successfully identified after only seven experimental verifications, indicating a notable enhancement in design efficiency.

In most of the existing studies, high-strength Cu–Ni–Si alloys were prepared by adding elements such as Co, Mg, Cr and titanium (Ti) to the alloy. For example, Zhang *et al.* designed a Cu–1.3Ni–1.4Co–0.56Si–0.03Mg alloy with a tensile strength of 858 MPa and an EC of 47.6% IACS via machine learning[11]. Guo *et al.* developed a Cu–3Ti–0.3Cr–0.15Mg alloy with an ultrahigh tensile strength (1,018 MPa) but a low EC (20.1% IACS)[37]. The EC of previously designed alloys generally lie below 52% IACS. In this study, the alloy composition was rapidly designed using machine learning and the NSGA-II multi-objective optimization algorithm. When added in trace amounts, Ag synergistically optimized the Cu–Ni–Si alloy system, conferring a considerable improvement in EC without compromising the strength. This new compositional-design strategy and material-selection scheme can realize high-strength, high EC copper alloys for integrated circuit lead frames.

Microstructural characterization and analysis of strengthening and conductive mechanisms

Microstructural characterization

In this section, representative alloys with the highest strength are selected from three alloy systems (Cr-only, Ag-only and Ag–Cr co-alloyed), namely, 2-alloy, 3-alloy and 5-alloy and characterized using SEM, EBSD, XRD and TEM. The results reveal the impacts of alloying elements on the morphology, precipitate distribution and corresponding strengthening mechanisms.

Figure 8A-C displays the SEM morphologies and energy-dispersive X-ray spectroscopy (EDS) results of alloys 2, 3 and 5, respectively. All three alloys exhibit disc-shaped and rod-shaped precipitates, with additional coffee bean-shaped precipitates in the 2- and 5-alloys. A preliminary EDS analysis of the SEM images [Supplementary Figures 4-6] revealed Ni, Co and Si enrichment in the disc- and rod-shaped precipitates and Cr enrichment in the bean-like precipitates. Next, the size distributions and area fractions of the precipitates were statistically measured in the three alloys. The 3-alloy (Cu–0.65Ni–1.65Co–0.44Si–0.09Mg

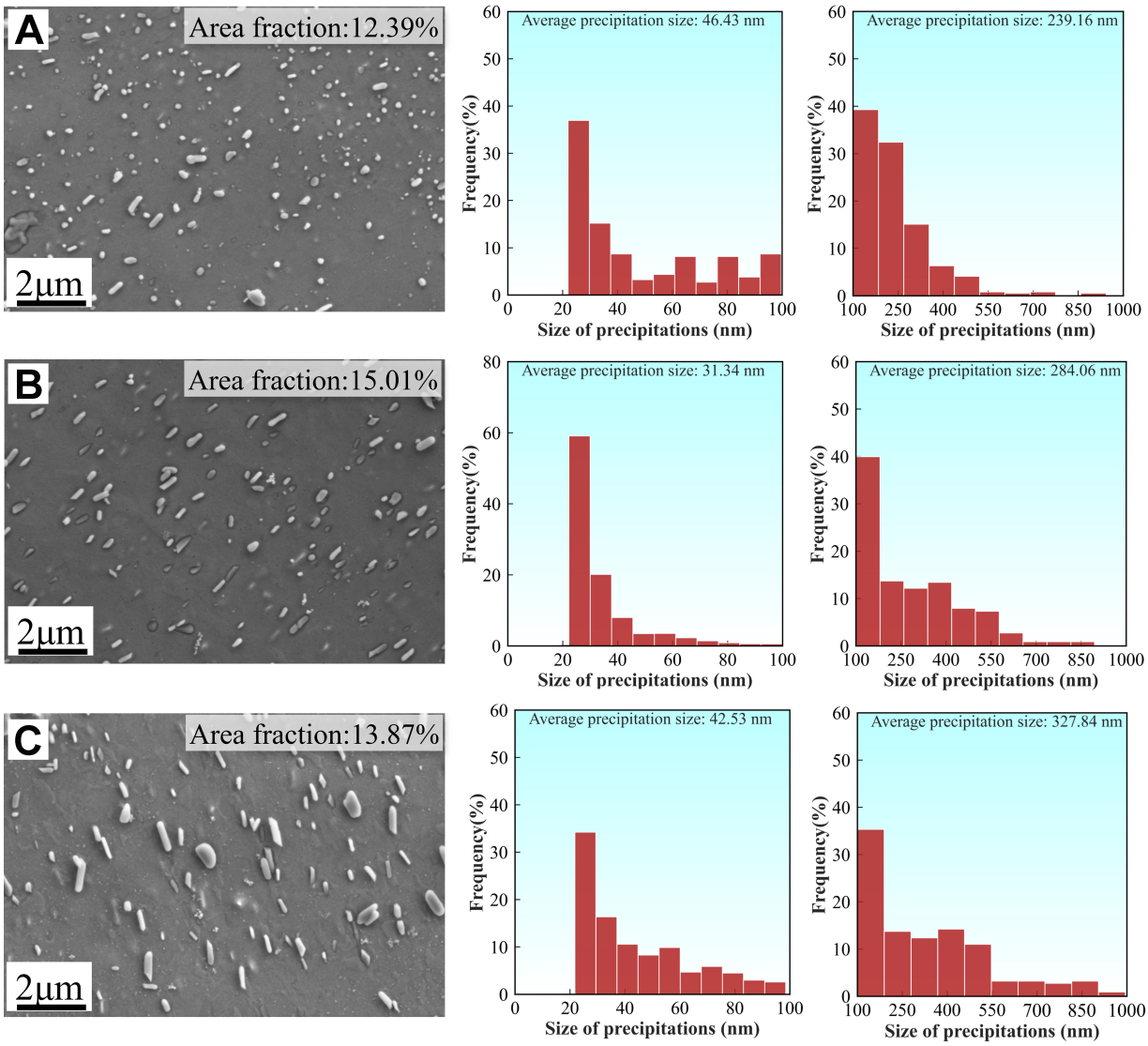

Figure 8. SEM images and size distribution charts of the precipitates from alloys 2, 3, and 5 at the end of the aging period: (A) 2-alloy (Cu–0.25Ni–1.71Co–0.47Si–0.14Mg–0.56Cr); (B) 3-alloy (Cu–0.65Ni–1.65Co–0.44Si–0.09Mg–0.46Ag); (C) 5-alloy (Cu–0.65Ni–1.72Co–0.48Si–0.14Mg–0.35Cr–0.09Ag). SEM: Scanning electron microscopy.

–0.46Ag) yielded the smallest average size of fine precipitates (31.34 nm) and the largest area fraction (15.01%) among the alloys.

Figure 9 shows the EBSD–inverse pole Fig orientation maps of alloys 2, 3 and 5. The grains are clearly stretched and fragmented along the rolling direction. The 3- and 5-alloys present smaller average grain sizes (0.64 and 0.65 μm, respectively) than the 2-alloy (0.70 μm).

Figure 10 presents the XRD diffraction patterns of alloys 2, 3 and 5. To compare the dislocation-strengthening contributions in the alloys, the average dislocation densities were determined via XRD-phase identification and micro-stress calculations. As lattice distortion broadens the diffraction peaks; the average microstrain in the alloys can be estimated from the variation of peak broadening with diffraction angle. The microstrain itself is closely related to dislocation density, which can be expressed by

$$\varepsilon = \frac{\beta * \cos\theta}{4\sin\theta} \tag{5}$$

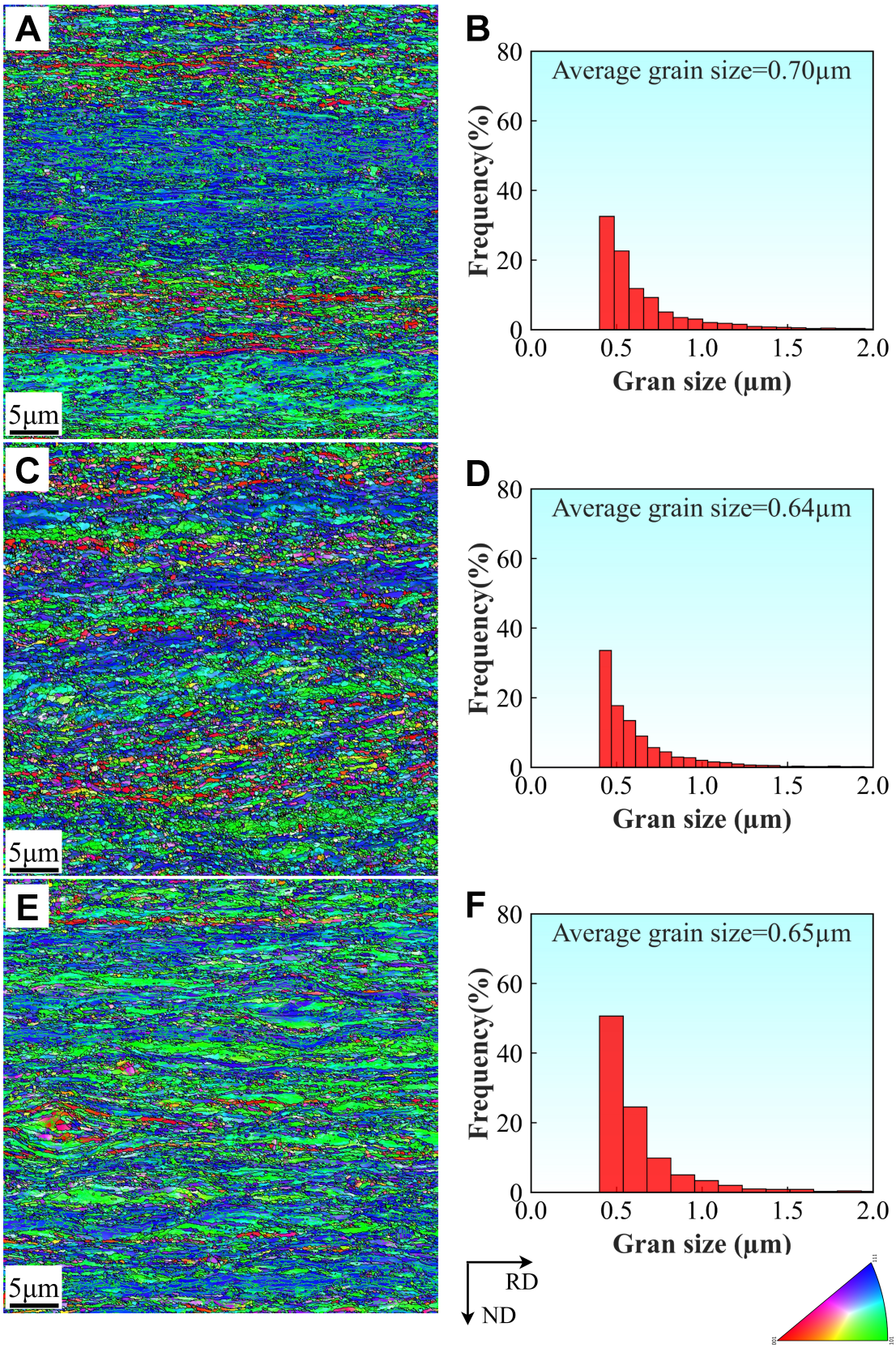

Figure 9. IPF and grain size diagrams of alloys 2, 3, and 5 after final aging. (A) 2-alloy (Cu–0.25Ni–1.71Co–0.47Si–0.14Mg–0.56Cr); (B) 3-alloy (Cu–0.65Ni–1.65Co–0.44Si–0.09Mg–0.46Ag; (C) 5-alloy (Cu–0.65Ni–1.72Co–0.48Si–0.14Mg–0.35Cr–0.09Ag). RD: Rolling direction; ND: normal direction.

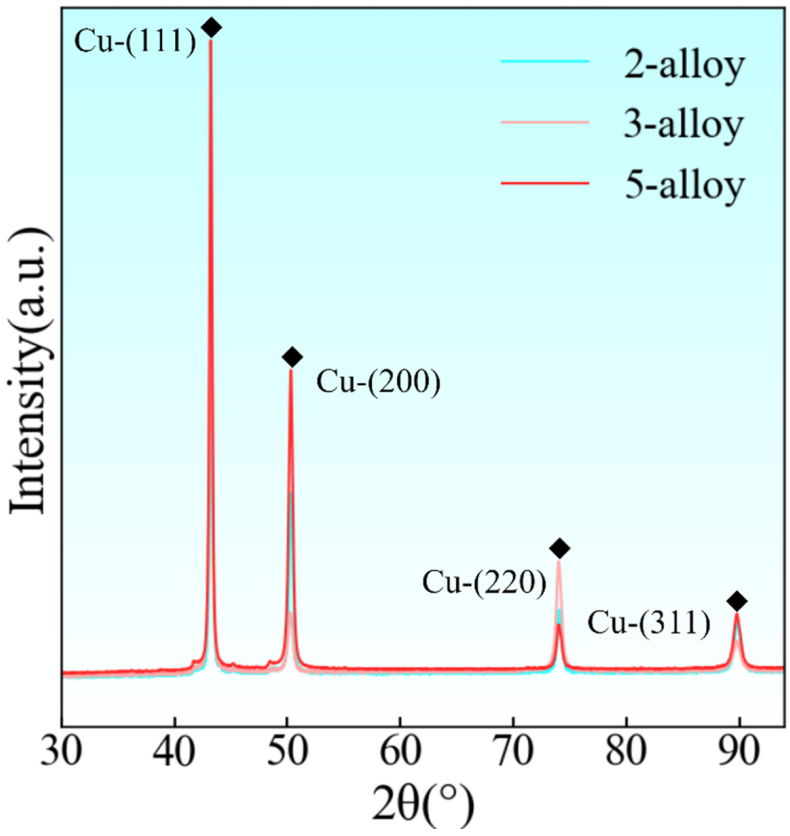

Figure 10. XRD patterns of alloys 2, 3, and 5 after final aging. 2-alloy: Cu–0.25Ni–1.71Co–0.47Si–0.14Mg–0.56Cr; 3-alloy: Cu–0.65Ni–1.65Co–0.44Si–0.09Mg–0.46Ag; 5-alloy: Cu–0.65Ni–1.72Co–0.48Si–0.14Mg–0.35Cr–0.09Ag. XRD: X-ray diffraction.

$$\rho = \frac{2\sqrt{3}\varepsilon}{d_G b} \tag{6}$$

The four strong diffraction peaks in the 30°-95° range correlate with the (111), (200), (220) and (311) crystal planes of Cu, respectively[38]. After fitting and analyzing the XRD diffraction peaks using Jade 6 software, the dislocation densities of the 2-, 3- and 5-alloys were determined as 4.66×10^{14}, 5.88×10^{14} and 5.39×10^{14} m^{-2}, respectively. The dislocation density was highest in the 3-alloy, indicating the most pronounced dislocation strengthening effect in this alloy.

Figure 11 shows the TEM morphologies and matching selected-area electron diffraction patterns of the 2-, 3- and 5-alloys (specific regions are labeled as "Area"). The relative orientation between the precipitates and the Cu matrix was determined as $[\bar{1},\bar{1},0]_{Cu}//[\bar{1},0,0]_{\delta},(1,\bar{1},0)_{Cu}//(0,\bar{1},\bar{2})_{\delta}$ in the 2-alloy (with disc-shaped precipitates), $[\bar{1},\bar{1},0]_{Cu}//[1,0,0]_{\delta},(1,\bar{1},\bar{1})_{Cu}//(0,1,\bar{2})_{\delta}$ in the 3-alloy (with rod-shaped precipitates) and $[0,\bar{1},\bar{1}]_{Cu}//[\bar{3},\bar{2},1]_{\delta},(1,\bar{1},\bar{1})_{Cu}//(0,1,\bar{2})_{\delta}$ in the 5-alloy (with rod-shaped precipitates). Together with the SEM-derived EDS results, the precipitates were identified as a predominant δ-$(Ni,Co)_2Si$ phase.

Figure 12 shows the TEM morphologies, dislocation and precipitate distributions and statistical precipitate-size results of the 2-, 3- and 5-alloys. TEM observations reveal extensive dislocation entanglement and a significantly higher dislocation density in the 3-alloy than in the 2- and 5-alloys, supporting the dislocation-density trend obtained from XRD fitting. EDS surface scanning [Figure 13] further indicates a high-density, uniformly dispersed distribution of nanoscale δ-$(Ni,Co)_2Si$ particles in the 3-alloy. The quantitative statistical analysis revealed a smaller average precipitate size (10.62 nm) and higher volume fraction (3.19%) in the

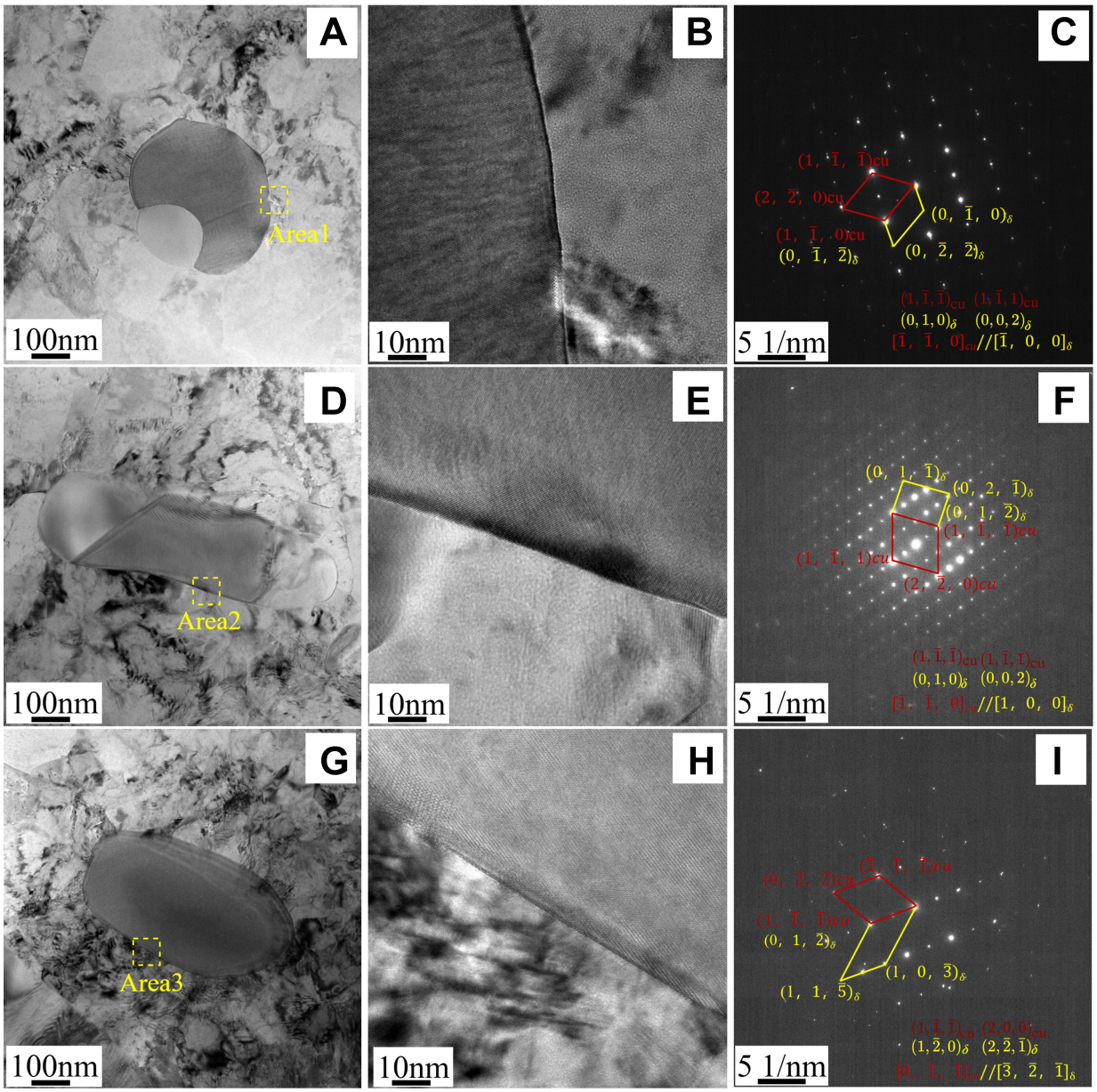

Figure 11. Bright-field, HRTEM and SAED images of alloys 2, 3, and 5 after final aging. (A-C) 2-alloy (Cu–0.25Ni–1.71Co–0.47Si–0.14Mg–0.56Cr); (D-F) 3-alloy (Cu–0.65Ni–1.65Co–0.44Si–0.09Mg–0.46Ag); (G-I) 5-alloy (Cu–0.65Ni–1.72Co–0.48Si–0.14Mg–0.35Cr–0.09Ag). HRTEM: High-resolution transmission electron microscopy; SAED: selected-area electron diffraction.

3-alloy than in the other alloys [Figure 12F]. The high-density dislocation entanglement synergizes with the uniformly distributed fine precipitates, enhancing both dislocation strengthening and precipitation strengthening. The yield strength and strength of the 3-alloy increase accordingly. Table 4 summarises the physical parameters (dislocation density, precipitation phase characteristics and grain size) obtained through the systematic characterization.

Strengthening mechanism

In the Cu alloy optimized through the NSGA-II algorithm, the increased yield strength stems from the synergistic interaction of multiple strengthening mechanisms, as expressed below:

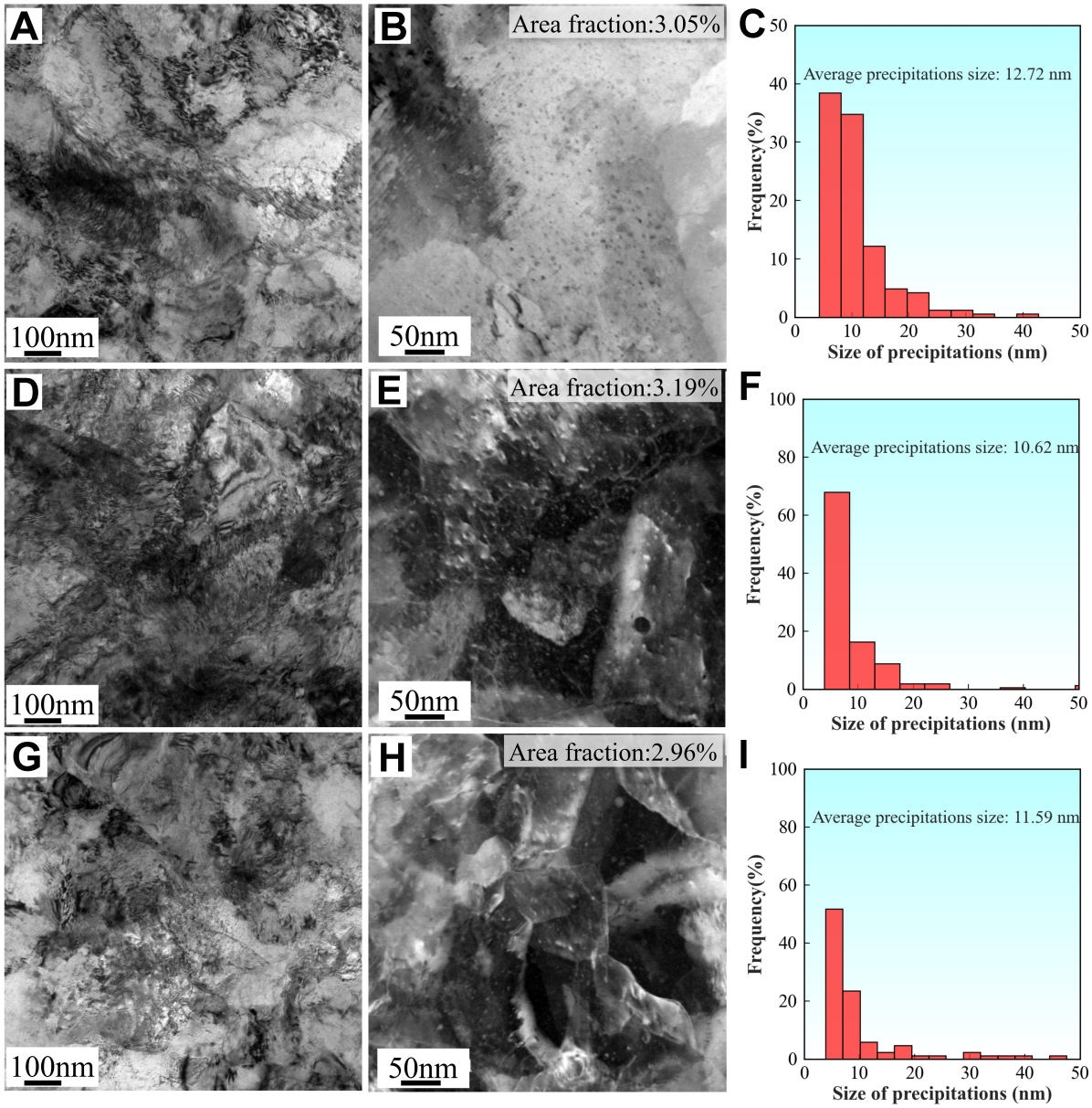

Figure 12. TEM images showing dislocation and precipitate distributions of alloys 2, 3, and 5 after final aging, along with precipitate size distribution charts. (A-C) 2-alloy (Cu–0.25Ni–1.71Co–0.47Si–0.14Mg–0.56Cr); (D-F) 3-alloy (Cu–0.65Ni–1.65Co–0.44Si–0.09Mg–0.46Ag); (G-I) 5-alloy (Cu–0.65Ni–1.72Co–0.48Si–0.14Mg–0.35Cr–0.09Ag). TEM: Transmission electron microscopy.

$$\sigma_{alloy} = \sigma_0 + \sigma_s + \sigma_d + \sigma_p + \sigma_g \tag{7}$$

Here, σ_0 represents the Peierls stress of copper (52 MPa)[38], and σ_s, σ_g, σ_p and σ_d denote the sources of the yield strength from solution strengthening, grain boundary strengthening, precipitation strengthening and dislocation strengthening, respectively[39]. The factors contributing to solid-solution strengthening are calculated using[40]:

$$\delta = \frac{|r_s - r_m|}{r_m} \tag{8}$$

$$\delta_s = \sum G\delta x_a^{\frac{3}{2}} \sqrt{\frac{x_a}{3}} \tag{9}$$

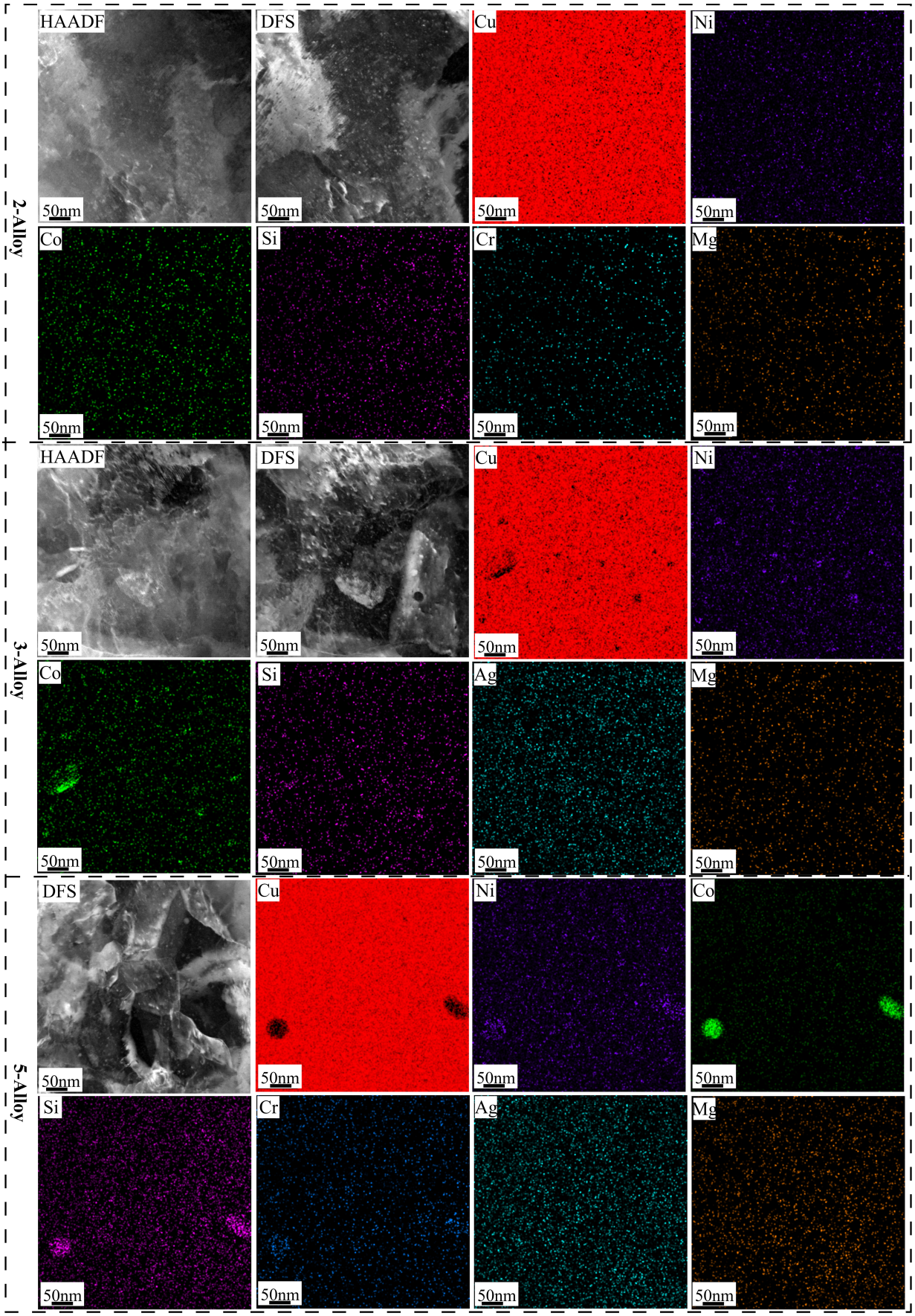

Figure 13. HAADF and dark field images of alloys 2, 3, and 5 after final aging, as well as EDS analysis results of each element. 2-alloy: Cu–0.25Ni–1.71Co–0.47Si–0.14Mg–0.56Cr; 3-alloy: Cu–0.65Ni–1.65Co–0.44Si–0.09Mg–0.46Ag; 5-alloy: Cu–0.65Ni–1.72Co–0.48Si–0.14Mg–0.35Cr–0.09Ag. HAADF: High-angle annular dark-field; EDS: energy-dispersive X-ray spectroscopy; DFS: dark-fields.

Table 4. For alloys 2, 3, and 5 after final aging: strain (ε), dislocation density (ρ), average precipitate size (d_p) and volume fraction (f_v), and grain size (d)

Alloy-Id	Dislocation		Precipitation		Grain
	ε (%)	ρ (10^{14}/m^{-2})	d_p (Nm)	f_v (%)	d (μm)
2	2.40	4.66	12.72	3.05	0.70
3	2.77	5.88	10.62	3.19	0.64
5	2.58	5.39	11.59	2.96	0.65

In Cu–Ni–Co alloys, the calculation is simplified by assuming that Co and Si exist as secondary precipitates, meaning that only Cr, Ni, Ag and Mg contribute to solid-solution strengthening. In the above equations, r_s and r_m denote the radii of the solute and Cu atoms, respectively, x_a is the molar fraction of the solute atom, δ is the lattice variation factor and G is the shear modulus of Cu (45.5 GPa)[41].

The grain boundary strengthening[41] is obtained by the Hall–Petch calculation:

$$\sigma_g = Kd^{-1/2} \tag{10}$$

where K is a constant equal to 0.18 Mpa·m$^{1/2}$, and d is the average grain diameter.

The contribution of precipitation hardening to the yield strength is calculated as[42,43]:

$$\lambda = \frac{1}{2}d_p * \sqrt{\frac{3\pi}{2f_v}} \tag{11}$$

$$\sigma_p = \frac{0.81MGb\ln(\frac{d_p}{b})}{2\pi(1-v)^{1/2}(\lambda - d_p)} \tag{12}$$

where b is the Burgers vector (0.255 nm), v is Poisson's ratio (0.34), M is the Taylor factor (3.1 for Cu alloys), λ is the effective interparticle spacing accounting for the size effect of the barrier and d_p and f_v are the average diameter and volume fraction of the precipitates, respectively; f_v is approximated by measuring the area fraction in TEM images using Image-Pro Plus software.

The yield strength attributed to dislocation strengthening is calculated as

$$\sigma_d = MG\alpha b\sqrt{\rho} \tag{13}$$

where α is a constant (= 0.2) and ρ is the dislocation density.

The theoretical yield strengths of the three samples designed through the Pareto strategy were calculated using Equation (7). Table 5 lists the yield-strength increments from each strengthening mechanism and compares the differences between the theoretical and experimentally measured values. The strength improvement in the three alloy specimens primarily stems from precipitation hardening and grain boundary hardening, with weaker contributions from dislocation hardening and solid-solution hardening [Figure 14].

Mechanism of electrical conductivity

The resistivities of other alloys using the IACS as a reference are calculated using[44]:

$$\rho_{alloy} = \frac{1.7241 * 10^{-6}}{\psi} \tag{14}$$

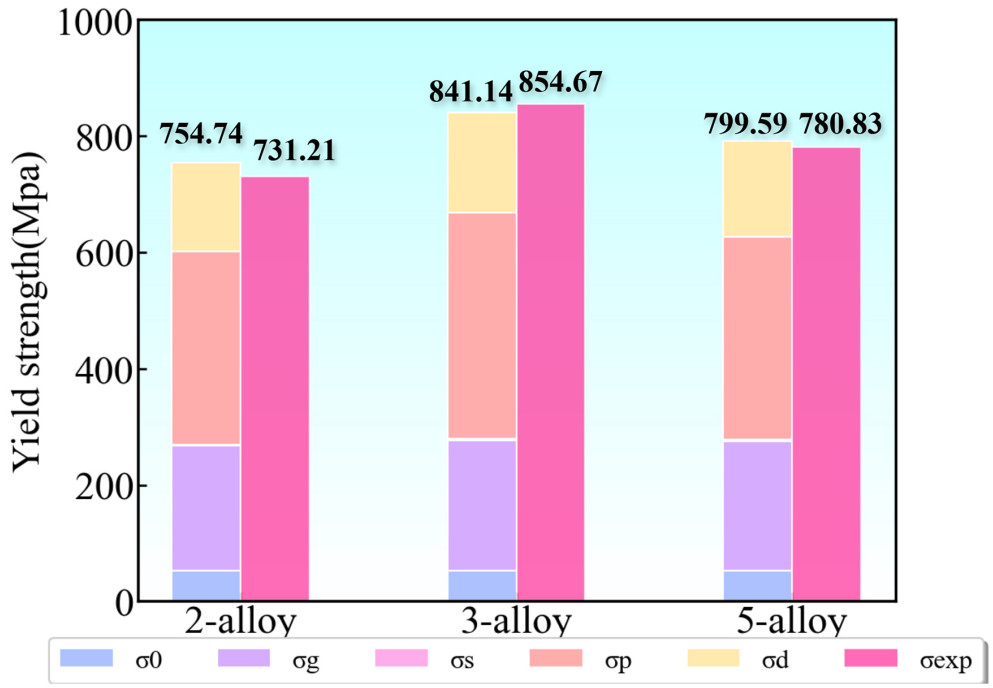

Figure 14. Comparison of experimental and calculated yield strength.

Table 5. Calculation of theoretical yield strength for alloys

Id	σ_0 (Mpa)	σ_g (Mpa)	σ_s (Mpa)	σ_p (Mpa)	σ_d (Mpa)	$\sigma_{calculate}$ (Mpa)	σ_{exp} (Mpa)	Error (%)
2	52	215.4	2.05	332.05	153.24	754.74	731.21	+3.22
3	52	225	2.3	389.66	172.18	841.14	854.67	-1.58
5	52	223.26	2.3	357.14	164.89	799.59	780.83	+2.40

where ψ represents the conductivity in %IACS, and ρ_{alloy} represents the resistivity of the alloy.

According to Matthiessen's rule[45], the resistivity of an alloy is influenced by microstructural features such as grain boundaries, dislocations and precipitates. The total resistivity is calculated as

$$\rho_{alloy} = \rho_0 + \rho_G + \rho_d + \rho_{ss} + \rho_p \tag{15}$$

where ρ_0 is the resistivity of pure Cu (1.72×10^{-8} Ω·m)[46], and ρ_G, ρ_d, ρ_{ss} and ρ_p represent the resistivity contributions of the grain boundaries, dislocations, solute atoms and precipitates, respectively. As the average spacing of the precipitated phases in the three designed alloys exceeds the mean free path of electrons in pure Cu (42 nm)[44], the precipitated phases will negligibly contribute to EC.

The resistivity change caused by dislocations is calculated as

$$\rho_d = \rho * A_d \tag{16}$$

where A_d is a constant (2.7×10^{-25} Ω·m^3)[43], and ρ is the dislocation density of the copper alloy.

The increase in resistivity caused by electron scattering at the grain boundaries is determined as

Table 6. The increments in resistivity and their respective contributions to the decrease in conductivity

Id	ρ_{alloy} (10^{-8} Ω.m)	ρ_d (10^{-10} Ω.m)	ρ_G (10^{-10} Ω.m)	ρ_{ss} (10^{-8} Ω.m)	$\Delta\psi_d$ (%IACS)	$\Delta\psi_G$ (%IACS)	$\Delta\psi_s$ (%IACS)
2	3.28	1.26	5.11	1.50	-0.38	-1.55	-45.56
3	2.91	1.59	5.59	1.12	-0.54	-1.91	-38.34
5	3.18	1.46	5.51	1.39	-0.46	-1.73	-43.6

IACS: International Annealed Copper Standard.

$$\rho_G = \frac{A_G}{d_G} \tag{17}$$

where A_G is a constant (= 3.58×10^{-16})[46], and d_G is the average grain size.

To determine the contribution of solute atoms to the resistivity ρ_{ss}, the resistivity contributions of the grain boundaries ρ_G, dislocations ρ_d and the pure copper matrix ρ_0 were subtracted from the overall resistivity of the alloy. Table 6 lists the effects of the various factors on the resistivity and conductivity $\Delta\psi$ of the alloy. The solute atoms exert the greatest adverse effect on the alloy's EC.

CONCLUSIONS

In this study, machine learning was combined with the NSGA-II algorithm to design novel high-strength, high-conductivity Cu-alloy compositions. The main conclusions are summarized below:

Optimal prediction models for UTS and EC with RMSE values of 57.89 MPa and 6.12% IACS, respectively, were developed by incorporating key alloy parameters such as sigma2 and delta_r. Subsequently, Bayesian hyperparameter optimization was integrated with the NSGA-II Pareto set strategy, achieving efficient optimization in the composition space. After fixing the multi-pass rolling and aging window based on our prior experience in process development, seven candidate compositions were rapidly screened for high-strength and high-conductivity Cu alloys. The mean absolute percentage error (MAPE) between the measured and predicted UTS values is 7.07%, and the maximum absolute error (MAE) is 12.41%. Meanwhile, the MAPE and MAE between the measured and predicted ECs are 7.84% and 17.18%, respectively. These results confirm the reliability of the "machine learning–multi-objective optimization–empirical synergy" design paradigm.

The proposed strategy successfully designed a Cu–0.65Ni–1.65Co–0.44Si–0.09Mg–0.46Ag alloy with a tensile strength of 868.63 MPa and an EC of 59.2% IACS. The primary strengthening mechanisms are precipitation hardening and grain refinement. Grain boundaries, dislocations and precipitates contribute limitedly to resistivity, and the solid solution of solute atoms predominantly contributes to the resistivity increase.

In the optimized alloy system, Ni, Co and Si interact synergistically with trace Ag and Mg. The composition is Ni+Co+Si = 2.74 wt%, with a (Ni+Co)/Si ratio of 5.23. The high unit price of Ag is offset by the very low total Ag content in the alloy; accordingly, the synergistic performance is improved at little additional cost. The existing C17200 alloy includes the expensive and toxic Be element and demands strict environmental and safety protections during smelting, processing and recycling. In contrast, the C70250 alloy contains no noble metals and contains cheaper raw materials than the Ag-containing alloy in this work, but its performance is inhibited by the strength–EC trade-off, which is largely overcome by the designed Ag-containing alloy.

DECLARATIONS

Authors' contributions

Writing - original draft, investigation: Li, Y.

Writing - review and editing, investigation: Xu, J.
Writing - review and editing, writing - original draft, investigation, formal analysis, data curation: Guan, B.
Formal analysis, investigation: Wu, D.; Han, Y.; Pan, X.; Xu, H.; Ma, G.
Formal analysis, supervision: Hu, Z.
Project administration, formal analysis: Hu, Q.

Availability of data and materials

The original contributions presented in this study are included in the article/Supplementary Materials. Further inquiries can be directed to the corresponding author(s).

AI and AI-assisted tools statement

During the preparation of this manuscript, the authors used GPT-Image-2 (released on 21 April 2026) for language editing and improving readability. In addition, GPT-Image-2 was used to assist in generating schematic illustrations, which was subsequently reviewed, edited, and incorporated into the final figures by the authors. These AI tools did not influence the study design, data collection, analysis, interpretation, or the scientific content of the work. All authors take full responsibility for the accuracy, integrity, and final content of the manuscript.

Financial support and sponsorship

The authors would like to thank the financial support from Key R&D Projects of Jiangxi Province (20261BCE310067), Jiangxi Key Laboratory of Advanced Copper-based Materials (2024SSY05021). The Article Processing Charge (APC) was fully funded by Shaanxi Sirui Advanced Materials Co., Ltd.

Conflicts of interest

All authors declared that there are no conflicts of interest.

Ethical approval and consent to participate

Not applicable.

Consent for publication

Not applicable.

Copyright

© The Author(s) 2026.

Supplementary Materials

Supplementary Materials

REFERENCES

1. Yang, L.; Zhang, F.; Yan, M.; Zhang, M. Microstructure and mechanical properties of multiphase layer formed during thermo-diffusing of titanium into the surface of C17200 copper–beryllium alloy. *Appl. Surf. Sci.* **2014**, *292*, 225-30. DOI
2. Xie, G.; Wang, Q.; Mi, X.; Xiong, B.; Peng, L. The precipitation behavior and strengthening of a Cu–2.0wt% Be alloy. *Mater. Sci. Eng. A.* **2012**, *558*, 326-30. DOI
3. Song, Y.; Yang, J.; Song, K.; et al. Effect of tensile stress annealing on residual stress and strength of C19400 alloy. *J. Mater. Res. Technol.* **2023**, *25*, 786-98. DOI
4. Zhou, F.; Zhang, Y.; Lu, L.; Song, K.; Gao, H. Effects of a thermal-ultrasonic stress relaxation process on the residual stress, mechanical properties and microstructures of C19400 copper alloy strips. *Mater. Sci. Eng. A.* **2022**, *841*, 143014. DOI
5. Yang, J.; Bu, K.; Zhou, Y.; et al. Influence of short-time annealing on the evolution of the microstructure, mechanical properties and residual stress of the C19400 alloy strips. *J. Alloys. Compd.* **2023**, *941*, 168705. DOI
6. Liao, W.; Yang, H.; Yi, C.; Zheng, J. Effect and mechanism of cold rolling and aging process on microstructure and properties of columnar grain C70250 copper alloy. *Mater. Sci. Eng. A.* **2022**, *833*, 142577. DOI
7. Liao, W.; Qiang, H.; Song, W.; Hu, Y.; Zhang, C. Effect and mechanism of room temperature rolling, cryogenic rolling and heat treatment on mechanical properties and electrical conductivity of Cu-Ni-Si alloy with continuous directional solidification. *J. Alloys. Compd.* **2023**, *949*, 169748. DOI

8. Liao, W.; Hu, Y.; Liu, Q. High strength and high electrical conductivity C70250 copper alloy with fibrous structure reinforced by high density, multi-scale nano-precipitates and dislocation. *Mater. Sci. Eng. A.* **2022**, *846*, 143283. DOI
9. Zhang, H.; Fu, H.; Sun, J.; Jiang, L.; Zhu, S.; Xie, J. Data-driven multi-process modeling and integrated design strategy for complex high-performance alloys. *Acta. Mater.* **2026**, *302*, 121648. DOI
10. Zhou, Y.; Yang, J.; Liu, Y.; et al. Ultrasonic vibration aging induces dislocation configuration evolution to achieve coordinated control of high strength and low residual stress of C70350 alloy strip. *Mater. Sci. Eng. A.* **2025**, *922*, 147655. DOI
11. Zhang, H.; Fu, H.; Zhu, S.; Yong, W.; Xie, J. Machine learning assisted composition effective design for precipitation strengthened copper alloys. *Acta. Mater.* **2021**, *215*, 117118. DOI
12. Li, Y.; Xu, J.; Guan, B.; et al. Design of Cu–Ni–Si alloy with ultra-high strength and high conductivity based on machine learning model. *J. Mater. Res. Technol.* **2026**, *42*, 8572-84. DOI
13. Yang, K.; Wang, Y.; Guo, M.; et al. Recent development of advanced precipitation-strengthened Cu alloys with high strength and conductivity: a review. *Prog. Mater. Sci.* **2023**, *138*, 101141. DOI
14. Zhang, Y.; Wang, Z.; Zhao, S.; et al. Effect of Cr addition on microstructure and properties of Cu-Ni-Co-Si-Mg alloys. *J. Alloys. Compd.* **2026**, *1050*, 185684. DOI
15. Pan, X.; Xu, J.; Guan, B.; et al. Synergistic enhancement of strength and conductivity of Cu-Ni-Co-Si alloys by Ag addition. *J. Alloys. Compd.* **2025**, *1040*, 183477. DOI
16. Deb, K.; Pratap, A.; Agarwal, S.; Meyarivan, T. A fast and elitist multiobjective genetic algorithm: NSGA-II. *IEEE. Trans. Evol. Comput.* **2002**, *6*, 182-97. DOI
17. Li, L.; Liu, G.; Yu, H.; et al. A machine learning strategy to achieve strength-conductivity-ductility synergy of high-performance Cu-Ni-Co-Si alloys via rolling and aging process. *J. Mater. Sci. Technol.* **2026**, *267*, 184-97. DOI
18. Li, R.; Kang, H.; Chen, Z.; et al. A promising structure for fabricating high strength and high electrical conductivity copper alloys. *Sci. Rep.* **2016**, *6*, 20799. DOI PubMed PMC
19. Zhao, Z.; Xiao, Z.; Li, Z.; Ma, M.; Dai, J. Effect of magnesium on microstructure and properties of Cu-Cr alloy. *J. Alloys. Compd.* **2018**, *752*, 191-7. DOI
20. Zhou, S.; Lei, Q.; Yin, J.; et al. Effect of Si addition on the microstructure and mechanical properties of a Cu-Cr-Ag alloy with high strength and electrical conductivity. *Mater. Sci. Eng. A.* **2025**, *934*, 148310. DOI
21. Qin, L.; Zhou, T.; Jiang, X.; et al. Microstructure and properties of Cu–Ni–Co–Si–Cr–Mg alloy by multistage thermomechanical treatment. *Trans. Nonferrous. Met. Soc. China.* **2023**, *33*, 3739-55. DOI
22. He, Z.; Lin, D.; Lau, T.; Wu, M. Gradient boosting machine: a survey. *arxiv* **2019**, arXiv:1908.06951. Available online: https://doi.org/10.48550/arXiv.1908.06951. (accessed 2026-11-23).
23. Xu, S.; Yang, K.; Chen, H.; Tan, J.; Gao, Y. Negative hypervolume improvement assisted infill criterion for multi-objective efficient global optimization and its applications. *Swarm. Evol. Comput.* **2025**, *99*, 102190. DOI
24. Rumelhart, D. E.; Hinton, G. E.; Williams, R. J. Learning representations by back-propagating errors. *Nature* **1986**, *323*, 533-6. DOI
25. de Ville, B. Decision trees. *WIREs. Comput. Stat.* **2013**, *5*, 448-55. DOI
26. Breiman, L. Stacked regressions. *Mach. Learn.* **1996**, *24*, 49-64. DOI
27. Cortes, C.; Vapnik, V. Support-vector networks. *Mach. Learn.* **1995**, *20*, 273-97. DOI
28. Chen, T.; Guestrin, C. XGBoost: a scalable tree boosting system. In *Proceedings of the 22nd ACM SIGKDD International Conference on Knowledge Discovery and Data Mining*. Association for Computing Machinery; 2016. pp. 785-94. DOI
29. Lundberg, S. M.; Lee, S. I. A unified approach to interpreting model predictions. In *Proceedings of the 31st International Conference on Neural Information Processing Systems (NIPS'17)*. Curran Associates Inc.; 2017. pp. 4768-77. DOI
30. Zhang, X.; Wu, H. Hesitant fuzzy linguistic Mahalanobis distance-based TOPSIS method for evaluating regional green development levels. *Appl. Soft. Comput.* **2025**, *173*, 112920. DOI
31. Ling, H.; Tang, Y.; Zhong, J.; Meng, X.; Zhang, M.; Zhang, L. Thermodynamic, diffusion and precipitation behaviors in Cu–Ni–Si–Co alloys: modeling and experimental validation. *J. Mater. Res. Technol.* **2025**, *35*, 3257-69. DOI
32. Li, Y.; Chen, S.; Wang, S.; Song, H.; Zhang, S. Coarsening mechanism of over-aged δ-Ni_2Si nanoscale precipitates in Cu-Ni-Si-Cr-Mg alloy. *Mater. Charact.* **2024**, *209*, 113693. DOI
33. Qin, Z.; Zhao, H.; Zhang, S.; et al. Design of high performance Cu-Ni-Si alloys via a multiobjective strategy based on machine learning. *Mater. Today. Commun.* **2024**, *39*, 108833. DOI
34. Fu, H.; Yin, Y.; Zhang, Y.; Zhang, M.; Yun, X. Enhancing the comprehensive properties of as-cast Cu–Ni–Si alloys by continuous extrusion combined with subsequent thermomechanical treatment. *Mater. Design.* **2022**, *222*, 111033. DOI
35. Shan, Y.; Zhang, C.; Zhang, Y.; et al. Influence of different rolling passes and deformation amounts on the microstructure evolution and strengthening mechanism of Cu–Ni–Si alloy. *J. Mater. Res. Technol.* **2024**, *33*, 3205-20. DOI
36. Monzen, R.; Watanabe, C. Microstructure and mechanical properties of Cu–Ni–Si alloys. *Mater. Sci. Eng. A.* **2008**, *483-4*, 117-9. DOI

37. Guo, X.; Li, L.; Liu, G.; et al. Microstructure and properties of Cu-3Ti-0.3Cr-0.15Mg alloy designed via machine learning. *Mater. Sci. Eng. A.* **2024**, *916*, 147344. DOI
38. Sitarama Raju, K.; Subramanya Sarma, V.; Kauffmann, A.; et al. High strength and ductile ultrafine-grained Cu–Ag alloy through bimodal grain size, dislocation density and solute distribution. *Acta. Mater.* **2013**, *61*, 228-38. DOI
39. Li, L.; Yu, H.; Yuan, Z.; et al. Hierarchical defect architectures enabled by Mg addition and cryogenic rolling for ultrahigh-strength Cu-Ni-Co-Si-Mg alloys. *Mater. Sci. Eng. A.* **2026**, *973*, 150686. DOI
40. Yasi, J. A.; Hector, L. G.; Trinkle, D. R. First-principles data for solid-solution strengthening of magnesium: from geometry and chemistry to properties. *Acta. Mater.* **2010**, *58*, 5704-13. DOI
41. Huang, J.; Xiao, Z.; Dai, J.; et al. Microstructure and properties of a novel Cu–Ni–Co–Si–Mg alloy with super-high strength and conductivity. *Mater. Sci. Eng. A.* **2019**, *744*, 754-63. DOI
42. Jiang, L.; Wang, C.; Fu, H.; Shen, J.; Zhang, Z.; Xie, J. Discovery of aluminum alloys with ultra-strength and high-toughness via a property-oriented design strategy. *J. Mater. Sci. Technol.* **2022**, *98*, 33-43. DOI
43. Taylor, G. I. The use of flat-ended projectiles for determining dynamic yield stress I. Theoretical considerations. *Proc. R. Soc. A.* **1948**, *194*, 289-99. DOI
44. Yun, P.; Fu, H.; Zhang, H.; Sun, J.; Zhao, M.; Xie, J. Rapid design of high-end copper alloy processes combining orthogonal experiments, machine learning, and Pareto analysis. *J. Mater. Res. Technol.* **2025**, *36*, 1005-16. DOI
45. Wang, C.; Fu, H.; Zhang, H.; He, X.; Xie, J. Simultaneous enhancement of mechanical and electrical properties of Cu–Ni–Si alloys via thermo-mechanical process. *Mater. Sci. Eng. A.* **2022**, *838*, 142815. DOI
46. Wang, X.; Xiao, Z.; Qiu, W.; Li, Z.; Liu, F. The evolution of microstructure and properties of a Cu–Ti–Cr–Mg–Si alloy with high strength during the multi-stage thermomechanical treatment. *Mater. Sci. Eng. A.* **2021**, *803*, 140510. DOI

Disclaimer/Publisher's Note: All statements, opinions, and data contained in this publication are solely those of the individual author(s) and contributor(s) and do not necessarily reflect those of OAE and/or the editor(s). OAE and/or the editor(s) disclaim any responsibility for harm to persons or property resulting from the use of any ideas, methods, instructions, or products mentioned in the content.

© The Author(s) 2026. Open Access This article is licensed under a Creative Commons Attribution 4.0 International License (https://creativecommons.org/licenses/by/4.0/), which permits unrestricted use, sharing, adaptation, distribution and reproduction in any medium or format, for any purpose, even commercially, as long as you give appropriate credit to the original author(s) and the source, provide a link to the Creative Commons license, and indicate if changes were made.